

# On the Rivers in the Euro-Atlantic Sky

Venugopal Thandlam (✉ [venux4@gmail.com](mailto:venux4@gmail.com))

Uppsala University <https://orcid.org/0000-0001-7771-1693>

Anna Rutgersson

Uppsala University, Centre of Natural Hazards and Disaster Science

Erik Sahlee

Uppsala University

---

## Article

**Keywords:** Atmospheric Rivers, North Atlantic Ocean, summer half-year, winter half-year, geopotential, surface latent heat flux, North Atlantic Oscillation and Scandinavian blocking

**Posted Date:** December 1st, 2020

**DOI:** <https://doi.org/10.21203/rs.3.rs-48633/v3>

**License:**  This work is licensed under a Creative Commons Attribution 4.0 International License.

[Read Full License](#)

---

# On the Rivers in the Euro-Atlantic Sky

Venugopal Thandlam<sup>1, 2, 3\*</sup>, Anna Rutgersson<sup>1,2</sup> and Erik Sahlee<sup>1</sup>

1. Department of Earth Sciences, Uppsala University, Sweden

2. Centre of Natural Hazards and Disaster Science, Uppsala, Sweden

3. Centre for Environment and Development Studies (CEMUS), Uppsala University, Sweden

\*corresponding authors' email: venu.thandlam@geo.uu.se

## Abstract

We study the spatiotemporal variability of Atmospheric Rivers (ARs) over Euro-Atlantic region using long-term reanalysis datasets. Winds, temperature and specific humidity at different pressure levels during 1979-2018 are used to study the water vapour transport integrated between 1000-300 hPa (IVT300) as a proxy to ARs. The intensity of ARs in the North Atlantic has been increasing in recent times (2009-2018) with large decadal variability and poleward shift ( $\sim 5^\circ$  towards the North) in landfall (1999-2018). Significant bias shown by different reanalysis products in IVT300 compared to ERA5 data is attributed to bias in specific humidity and winds. Different reanalysis datasets show similar spatial patterns of IVT300 in mapping ARs but has a bias of around  $40\text{-}60 \text{ kgm}^{-1}\text{s}^{-1}$  compared to ERA5. The magnitude of winds and specific humidity in the lower atmosphere (below 750 hPa) dominates the total column water vapour and intensity of ARs in the north Atlantic. IVT300 in all reanalysis datasets in the North Atlantic show a standard deviation of  $200 \text{ kgm}^{-1}\text{s}^{-1}$  which is around 60% of the IVT300 climatology ( $>300 \text{ kgm}^{-1}\text{s}^{-1}$ ). Though ARs have higher frequency of landfalling over Western Europe in winter half-year

24 (WHY); the intensity of IVT300 in winter is 3% lower than the annual mean. On the other hand,  
25 lower frequency of ARs in summer half-year (SHY) shows 3% higher intensity than the annual  
26 mean. There is a significant impact of the North Atlantic Oscillation (NAO) and Scandinavian  
27 blocking on the location of landfall of ARs. Furthermore, there is a strong latitudinal dependence  
28 of the source of moisture flux in the open ocean, contributing to the formation and enhancing AR's  
29 strength.

30  
31 **Keywords:** Atmospheric Rivers, North Atlantic Ocean, summer half-year, winter half-year,  
32 geopotential, surface latent heat flux, North Atlantic Oscillation and Scandinavian blocking.

### 34 **Introduction**

35 Tropospheric atmospheric dynamics are guided by water vapour in the lower atmosphere  
36 (Schneider et al., 1999). Particularly, heat and momentum in the lower troposphere have strong  
37 coupling with the movement of moisture in the troposphere. Hence, it is essential to study the  
38 tropospheric moisture transport to better understand the global water cycle, synoptic weather  
39 patterns and climate change due to enhanced evaporation in recent decades and global warming  
40 (Trenberth, 2011). Also, the ocean and atmosphere play a key role in transporting heat and water  
41 vapour poleward, respectively. Atmospheric general circulation plays a vital role in circulating  
42 water vapour in the lower troposphere. The large-scale land-ocean atmospheric exchange of water  
43 demonstrates the coupling of the atmospheric branch of the hydrological cycle (Hack et al., 2006).  
44 The global and continental-scale transport of water vapour has important implications for climate  
45 variability and hydrology (Brubaker et al., 1994). Hence, atmospheric scientists must consider  
46 studying climatological, meteorological and hydrological aspects of the transport of moisture in

47 the lower atmosphere (Gimeno 2013; Gimeno et al., 2012). It is particularly important to  
48 understand conceptual models of moisture transport to aid research into the origin of continental  
49 precipitation (Gimeno 2014). Also, moisture transport in mid-latitudes plays a key role in guiding  
50 the global atmosphere and climate dynamics in various temporal and spatial scales.

51 Most of the meridional water vapour transported across midlatitudes (90% of the total mid-latitude  
52 vertically integrated water vapour flux) takes place through narrow corridors in less than 10% of  
53 the zonal circumference. These narrow filaments of poleward water vapour transport are termed  
54 as atmospheric rivers (ARs) (Yong and Newell 1998; Ralph et al. 2004). These transient  
55 filamentary regions occur within the warm conveyor belt of extratropical cyclones in a maritime  
56 environment and are characterized by high water vapour content and strong low-level winds  
57 (Ralph et al. 2004, 2005, 2006). Thus, these corridors tend to be quite narrow (<1000 km wide)  
58 relative to their length scale (>2000 km) (Neiman et al., 2008). The warm conveyor belt transports  
59 both sensible and latent heat, particularly the later contributes to the poleward heat transport that  
60 occurs in the form of water vapour flux from the warm sea surface over oceanic regions serving  
61 as a major moisture source. Most of the water vapour transport within these rivers occurs in the  
62 lowest 2.5 km of the atmosphere due to moist-neutral stratification (Ralph et al. 2005). Hence,  
63 these are also called tropospheric rivers due to their occurrence in the lower troposphere (Yong  
64 and Newell 1994, 1998). The combination of lower tropospheric moist neutrality, strong horizontal  
65 winds, large and concentrated water vapour content yields an occurrence of heavy orographic  
66 precipitation and winds on elevated terrain, which can lead to severe and widespread flooding  
67 (Ralph et al. 2006; Neiman et al. 2002, 2011; Ruby and Qian 2009; Lavers et al., 2011, 2012;  
68 Waliser and Guan, 2017; De Luca et al., 2017), and could further cause landslides to occur over  
69 the adjacent area (Jason et al., 2019). Heavy and untimely precipitation (Kritika et al., 2018; Yan

70 et al., 2018) from warm ARs also causes preexisting snowpack to melt in high latitudes and poles  
71 allowing freshwater inflow into oceans and contribute to the sea level rise (Neff William, 2018;  
72 Mattingly et al., 2018), leading to coastal flooding (Khouakhi and Villarini 2016). Snowmelt and  
73 intense flooding due to ARs could change the geomorphic processes, biodiversity and mass  
74 mortality of wildlife (Joan et al., 2015; Brian et al., 2016). Conversely, ARs could also change the  
75 ice sheet surface mass balance over poles by 74-80% through heavy snow accumulation (Irina et  
76 al., 2014). Thus, ARs are key to understanding extratropical and polar hydro-climate features  
77 through polar warming, sea ice melt, and precipitation (Deanna et al., 2018; Kensuke et al., 2018).  
78 Consequently, these mesoscale filamentary features play a key role in the global water cycle and  
79 represent an important phenomenon linking weather and climate.

80           There are numerous studies over midlatitudes documenting the AR characteristics, landfall,  
81 and their relationship with the extreme hydrometeorological events (De Luca et al., 2017). Many  
82 studies have focused on ARs over the Pacific; particularly on the south-west coast of the United  
83 States (Ralph et al., 2006, 2019, 2005, 2006; Neiman et al., 2008; Chapman et al., 2019, and the  
84 references therein) and South America (Viale and Nunez, 2011). There are a few studies aimed at  
85 the global characteristics of ARs (Waliser and Guan 2017; Guan and Waliser 2017, 2015).  
86 Recently there is an increasing focus on the precipitation over Europe and ARs over the North  
87 Atlantic (Pasquier et al., 2019; Yang et al., 2016; Lavers et al., 2016; Champion et al., 2015).  
88 Recent studies in Asia (Kritika et al., 2018; Yang et al., 2018; Youichi et al., 2017) and Africa  
89 (Blamey et al., 2018; Alexandre et al., 2018) have focused on the relationship between ARs and  
90 extremes in precipitation. However, the study of ARs over the North Atlantic and Europe needs  
91 more attention due to potentially increasing extremes in hydrometeorological events such as  
92 snowfall, precipitation and flooding (Millán 2014; Kundzewicz et al., 2006; Van den Besselaar et

93 al., 2013). Most of the extreme wind events catalogued between 1997 and 2013 over Europe with  
94 billion US dollar losses were associated with ARs (Waliser and Guan 2017). Hence, it is essential  
95 to study both oceanic and atmospheric processes affecting these anomalies and extremes. AR is  
96 one such feature guided by both oceanic and atmospheric dynamics and causes extremes in  
97 precipitation and influences the hydrology over Europe. Lavers et al., (2013) studied the  
98 relationship between ARs and extreme precipitation across Europe and found that the North  
99 Atlantic Oscillation (NAO) has a significant impact on precipitation caused by ARs. The same  
100 study highlighted anomalies in central European precipitation patterns caused by ARs over the  
101 North Atlantic. According to a multi-model ensemble of the Coupled Model Intercomparison  
102 Project (CMIP5); AR frequency is projected to increase 127%-275% by the end of this century, at  
103 peak AR frequency regions ( $45^{\circ}$ - $55^{\circ}$ N) over Europe, under the representative concentration  
104 pathway 8.5 (RCP8.5) scenario. This enhanced frequency is associated with the wind changes in  
105 the midlatitude jet (Yang et al., 2016). ARs cause 20-30% of all precipitation in parts of Europe  
106 and the United States, however with strong seasonality. Also, ARs penetrate further inland over  
107 Europe than over the United States (Lavers and Villarini 2015). On the other hand, ARs are in  
108 sync with the largest floods over Western Europe and the United Kingdom (Lavers et al., 2011,  
109 2012; De Luca et al., 2017).

110 Several procedures are in practice to detect, track and forecast ARs in advance using  
111 observational, reanalysis, and numerical models (Ralph et al., 2019; Fish et al., 2019; Lavers et  
112 al., 2018). Integrated Water Vapor (IWV) (Ralph et al., 2004; Neiman et al., 2008b; Guan et al.,  
113 2010) and integrated vapour transport (IVT) (Zhu and Newell, 1998; Roberge et al., 2009; Jiang  
114 and Deng, 2011) are the two most common techniques used to define, detect and track ARs. Time  
115 integrated IVT, Meteograms and cross-sections are some other methods to study ARs. Both IWV

116 and IVT consider vertically integrated (between 1000 hPa to 300 hPa or less) horizontal water  
117 vapour transport (significant poleward moisture transport) as a proxy to AR occurrence when the  
118 standardized IVT was greater than a threshold (Roberge et al. 2009). Accurate atmospheric  
119 parameters such as winds, specific humidity, and the temperature at different pressure levels  
120 obtained from satellites and reanalysis products are essential to study ARs (Neiman et al., 2009;  
121 Dettinger, 2011). Though necessary parameters are available from different platforms,  
122 atmospheric reanalysis is the best estimate of the historical state of the Earth's atmosphere. These  
123 datasets are produced by assimilating meteorological/oceanic observations into numerical weather  
124 prediction model output. In this work, we aim to study the characteristics of ARs over the North  
125 Atlantic such as spatiotemporal variability, bias in mapping ARs using different reanalysis  
126 products, frequency and decadal variability of ARs. The objective of this study is also to look at  
127 the variability and trend of ARs in the North Atlantic in relation to the different atmospheric  
128 parameters and IVT in different layers of the atmosphere. The spatial/horizontal resolution  
129 dependence of ARs over the North Atlantic from different reanalysis products was computed with  
130 reference to IVT300 mapped using ERA5. The paper is organized as follows. Section 2 describes  
131 the data and methods, followed by results and discussions in section 3 and conclusions in section  
132 4.

### 133 **Data and Methods**

134 We have used six-hourly winds, temperature, and specific humidity data at different  
135 pressure levels from six reanalysis products available during 1979-2018. These six reanalysis  
136 datasets include 20th Century Reanalysis version 2 (20CR-V2) from the NOAA Earth System  
137 Research Laboratories (ESRL), ERA-Interim, ERA5 from the European Centre for Medium-  
138 Range Weather Forecasts (ECMWF), Modern-Era Retrospective analysis for Research and

139 Applications (MERRA-2) from National Aeronautics and Space Administration (NASA), Climate  
140 Forecast System Reanalysis version 2 (CFSR-v2), NCEP-NCAR Reanalysis version 2 from the  
141 National Center for Environmental Prediction (NCEP). Apart from MERRA-2, which has been  
142 available since 1980; all datasets are available from 1979 and have different spatial resolutions.  
143 Details of reanalysis datasets are given in table 1. In addition to traditionally mapping ARs using  
144 both IVT (Equation 2) and IWV (Equation 4), we also included the temperature of corresponding  
145 layers in these algorithms to normalize the computed IVT (nIVT, Equation 3) and IWV (nIWV,  
146 Equation 5) and study the difference from the normal approach using different reanalysis products  
147 and compared these two methods in the Atlantic. Temperature normalization is done to understand  
148 the change in the thermodynamic component of IVT and IWV using the Clausius-Clapeyron  
149 equation (1), which states that the water-vapour content of saturated air,  $q^*$ , increases nearly  
150 exponentially with temperature  $T$  (Payne et al., 2020).

$$151 \quad \frac{dq^*}{dT} = \alpha(T)q^* \quad (1)$$

152  $\alpha(T)$  is the Clausius-Clapeyron scaling factor, defined as

$$153 \quad \alpha(T) = \frac{L}{R_v T^2}$$

154 where  $L$  is the latent heat of vaporization and  $R_v$  is the gas constant of water vapour. Within the  
155 saturated environment at the core of an AR where  $q \approx q^*$ , a small change in the surface warming  
156 would cause specific humidity to further increase. Thus, specific humidity in the upper layers of  
157 the atmosphere strongly depends on the increase in layer's temperature due to increasing surface  
158 temperature and the Clausius-Clapeyron scaling factor,  $\alpha(T)$  and is approximately  $6.6\% \text{ K}^{-1}$  for  
159 surface temperatures causing ARs that are land-falling over California in the present climate ( $T =$   
160  $13^\circ\text{C}$ ) (Dettinger 2011; Gonzales et al., 2019).

161

162 Integrated Vapor Transport (IVT):

$$163 \quad IVT = g^{-1} \sqrt{\left(\int_{1000}^p QU dp\right)^2 + \left(\int_{1000}^p QV dp\right)^2} \quad (2)$$

164

165 Normalized IVT:

$$166 \quad nIVT = g^{-1} \sqrt{\left(\int_{1000}^p \frac{QU}{T} dp\right)^2 + \left(\int_{1000}^p \frac{QV}{T} dp\right)^2} \quad (3)$$

167

168 Integrated Water Vapor (IWV):

$$169 \quad IWV = g^{-1} \int_{1000}^p Q dp \quad (4)$$

170

171 Normalized IWV:

$$172 \quad nIWV = g^{-1} \int_{1000}^p \frac{Q}{T} dp \quad (5)$$

173

174 Where Q is specific humidity in  $\text{kgkg}^{-1}$ , U and V are zonal and meridional components of winds  
175 at different pressure levels measured in  $\text{ms}^{-1}$ , P is the desired pressure (hPa) up to which the  
176 atmospheric parameters are integrated; g is the acceleration due to gravity, which is a constant and  
177 is given as  $9.8 \text{ ms}^{-2}$  (Neiman et al., 2008a; Lavers and Villarini, 2013a, 2013b). Normalization  
178 with temperature is done by dividing Q, U and V with the temperature at a corresponding pressure  
179 level. Supplementary table S1 shows the details of the variables and their units. Thus, time-  
180 integrated (00, 06, 12, and 18) daily ARs data has been generated from six-hourly reanalysis  
181 datasets using IVT ( $\text{kgm}^{-1}\text{s}^{-1}$ ), normalized IVT ( $\text{kgm}^{-1}\text{s}^{-1}\text{K}^{-1}$ ); IWV (mm) and normalized IWV  
182 ( $\text{mmK}^{-1}$ ) from the surface to 750 hPa, 500 hPa and 300 hPa. Quantification of ARs over the North  
183 Atlantic was done using the climatology and standard deviation for different methods. This is

184 essential to see the spatial variability including the magnitude of water vapour transport over the  
185 North Atlantic and into Western Europe. We have used the AR detection method from Lavers and  
186 Villarini (2013b).

187         The time-integrated (00, 06, 12, and 18) daily AR data have been used in further analysis  
188 to study temporal and spatial variability of ARs over the North Atlantic, both in climatic and  
189 decadal timescales. In addition to studying biases in different atmospheric parameters, the annual  
190 and seasonal climatology and strength of ARs at different layers were studied. For the  
191 intercomparing of reanalysis datasets, we consider ERA5 as the reference dataset because of its  
192 enhancements in parameterization and resolution. Furthermore, the study focuses on the variability  
193 of ARs intensities in different products, including major categories of ARs and their frequencies  
194 in the North Atlantic. Linear regression analysis with student t-test done in the study helps to  
195 understand the spatial trend in the IVT300 (ARs); followed by the study to understand the state of  
196 the atmosphere using atmospheric parameters to describe the characteristics of land-falling of ARs.

197         A general approach used to map ARs is using IVT300 by considering pressure levels from  
198 surface (1000 hPa) to 300 hPa (Neiman et al., 2008b; Guan et al., 2010, Lavers et al., 2011). A  
199 few studies also considered 900 hPa as the surface reference level (Gorodetskaya et al., 2014); 500  
200 hPa (Yang et al., 2016) and 200 hPa (Sellars et al., 2017; Mattingly et al., 2018) as upper limits.  
201 Shields et al., (2018) compiled all available methods including thresholds to map ARs globally as  
202 a part of describing the Atmospheric River Tracking Method Intercomparison Project (ARTMIP).  
203 Hence, there is persisting ambiguity in using reference pressure levels to map ARs. Therefore, here  
204 we quantify the magnitude of annual and semi-annual IVT in different layers. For this purpose,  
205 the total column (1000-300 hPa) has been divided into sub-layers consisting 500-300 hPa  
206 (IVT\_Upper), 750-300 hPa (IVT\_Middle), 750-500 (IVT\_Lower) which lie above 750 hPa

207 pressure level in addition to computing IVT500 (1000-500 hPa) and IVT750 (1000-750 hPa). This  
208 exercise helps to map the strength of IVT and spatial variability in these layers, which is a function  
209 of exponentially decreasing water vapour pressure with height.

## 210 **Results and Discussions**

### 211 **Climatology and standard deviation of ARs over the North Atlantic:**

212 The annual climatology from ERA5 daily data using IVT and nIVT methods shows the  
213 highest AR intensity in the region enclosed between 30°N-60°N (Figure 1). Though the intensity  
214 of AR varies from event to event, on average IVT300 (IVT between 1000-300 hPa) (Figure 1a)  
215 over the North Atlantic is around  $300 \text{ kgm}^{-1}\text{s}^{-1}$  and is in line and directed along with the westerly  
216 wind over this region. The maximum nIVT300 (nIVT between 1000-300 hPa) over the North  
217 Atlantic is in coherence with the maximum IVT300 and along the same path with maximum values  
218 ( $>1 \text{ kgm}^{-1}\text{s}^{-1}\text{K}^{-1}$ ) concentrated over the central North Atlantic (Figure 1b). The nIVT300 is  
219 accounted for available IVT300 per unit temperature, is a proxy to fractional changes in available  
220 specific humidity in the atmospheric column per degree of atmospheric warming. In upper layers  
221 of the atmosphere,  $\alpha$  varies with the varying temperature. Hence,  $\alpha$  increases with the decreasing  
222 temperature with height and amplifies changes in the specific humidity aloft and is larger in the  
223 upper troposphere. On the other hand, increasing specific humidity in upper layers tends to release  
224 more latent heat flux with ascending air, and decrease the lapse rate with warming and thus  
225 increasing the temperature with height. If the vertical column of the atmosphere is saturated and  
226 has moist-neutral conditions, the combination of these factors implies a rate increase in IVT that  
227 is substantially larger than that of near-surface water vapour (Payne et al., 2020). Hence, a  
228 fractional change in IVT is a reasonable approximation to the thermodynamic contribution to IVT  
229 change. Thus, on top of concentrated warm coastal surface waters due to Gulf stream over western

230 North Atlantic causing higher evaporation; specific humidity advecting from tropics could be  
231 saturating the upper troposphere over the central North Atlantic and showing higher IVT300 and  
232 nIVT300.

233         Though AR mapping and characteristics study initially was started using IWV, the  
234 importance of tracking the AR made IVT as a widely used method. However, using IWV would  
235 give estimation of concentration of total column condensable water vapour at a given instance  
236 (Ralph and Dettinger 2011; Gimeno et al., 2014). Climatology of IWV300 (IWV between 1000-  
237 300 hPa) (Figure 1c) and nIWV300 (nIWV between 1000-300 hPa) (Figure 1d) shows the gradient  
238 of water vapour varying from a maximum at the equator and fading towards the pole. Using nIWV  
239 here shows the amount of total column condensable water vapour per degree Kelvin. The amount  
240 of evaporation caused by solar heating and strength of the near surface winds determines the extent  
241 and the scale of the water vapour. However, the occurrence of AR over a region and its magnitude  
242 guided by the amount of precipitable water vapour are not only bound to the availability of specific  
243 humidity in the atmosphere but also on the magnitude and direction of winds carrying the water  
244 vapour. Hence, the higher intensity of ARs over the North Atlantic and Western Europe are in the  
245 direct vicinity of the region of occurrence of extratropical cyclones and associated strong surface  
246 wind speeds (Pinto et al., 2013; De Luca et al. 2017) and along the path of the subtropical westerly  
247 winds. Although all the methods used in mapping ARs show higher values over the western North  
248 Atlantic, the origin of ARs and the region of moisture flux into ARs in this part of the ocean are  
249 still debatable. These elongated features are also affected by the synoptic weather conditions, and  
250 their magnitude depends on the midway convergence of water vapour flux from adjacent areas.  
251 Despite IVT300 climatology showing a maximum of  $300 \text{ kgm}^{-1}\text{s}^{-1}$ , each AR could be different in  
252 magnitude and its strength varies as per the state of the atmosphere at a given instance.

253 One example of an AR from 6<sup>th</sup> March 2002 mapped using four different methods in Figure  
254 2 has IVT300 higher than 500 kgm<sup>-1</sup>s<sup>-1</sup> (Figure 2a). This event was one of the intense ARs that  
255 occurred over northern Europe and caused excess rainfall over Britain and southern Scandinavia.  
256 While the IVT300 is narrow and short, nIVT300 (Figure 2b) shows the adjacent regions saturated  
257 with water vapour. The advected moisture from these surrounding regions could enhance the  
258 intensity and lifetime of the AR over a given location. Thus, nIVT300 is a useful method in  
259 mapping the true characteristics and saturated water vapour content in AR. Similarly, IWV300 and  
260 nIWV300 (Figures 2c, 2d) for this event show the origin of AR and the source of the advection,  
261 which is, in this case, occurred from the warm tropical region (20°N) enriched with high specific  
262 humidity.

### 263 **AR intensity and bias in reanalysis data**

264 In the North Atlantic, different reanalysis products used to map the ARs show variability  
265 in magnitudes (Figure 3). The climatology (shaded) and standard deviation (contours) of ERA5  
266 (Figure 3a) has lower IVT300 intensity than any other reanalysis products used; while ERA-  
267 Interim has higher climatology (intensity) and standard deviation. The highest variability (standard  
268 deviation of 200 kgm<sup>-1</sup>s<sup>-1</sup>) is around 60% of the maximum values of climatology (>300 kgm<sup>-1</sup>s<sup>-1</sup>)  
269 in all reanalysis datasets. Both climatology and standard deviation of IVT300 are higher in JJA  
270 and lower in MAM and has strong variability (Supplementary Figure 1a, 1b), and all reanalysis  
271 products show similar patterns (Figure 3a-3f). Although these values vary with seasons, both SON  
272 and DJF have longer stretch/extent of higher climatology and standard deviation values in the  
273 North Atlantic. Similarly, both these values have large spread and reaching Western Europe in  
274 winter half-year (WHY or ONDJFM), showing a high frequency of ARs during this time (Lavers

275 et al., 2011, 2012). Low frequency in summer half-year (SHY or AMJJAS) mainly concentrated  
276 over the central Atlantic.

277 All reanalysis data sets are developed using numerical and statistical approaches integrated  
278 with observations with possible bias corrections. Thus, all these reanalysis datasets show a similar  
279 spatial pattern over the North Atlantic, but the difference in magnitudes is explained by the  
280 variability in the magnitudes of Q, U and V, which could be further due to bias in observations,  
281 discrepancies in product development. To illustrate it further, we compared the atmospheric  
282 parameters used (Q, U, and V) to map AR in 20CR (coarse resolution) with the ERA5 (high  
283 resolution data) (Figure S3). A simple interpolation is used to match grids points of parameters in  
284 ERA5 with 20CR data as these data sets have a different spatial resolution. The climatology of  
285 these individual parameters during 1979-2014 shows that 20CR overestimating (ERA5-20CR) the  
286 magnitude (Figures S3d-S3f) compared to the ERA5 (Figures S3a-S3c). Hence, the 20CR data has  
287 a bias of  $0.5 \text{ gKg}^{-1}$  in Q,  $1 \text{ ms}^{-1}$  in U and V components of wind in the North Atlantic (Figures  
288 S3g-S3i). However, this would not be obvious for different seasons and different ARs in the  
289 Atlantic due to strong seasonal variability of IVT300 intensities and atmospheric state which  
290 makes each AR unique event.

291 In the case of AR mapped on 6<sup>th</sup> March 2002, different reanalysis products show significant  
292 bias in IVT300 compared to ERA5 (Figure 4). Both MERRA and ERA-Interim show positive bias  
293 at the head of the AR (AR path is marked as the grey arrow in Figure 4) and negative bias in the  
294 tail (Figure 4a, 4b). On the other hand, NCEP (NCAR, CFS) and 20CR have a strong negative bias  
295 on aggregate (Figures 4c-4e). Both these positive and negative biases are around  $50 \text{ kgm}^{-1}\text{s}^{-1}$  in  
296 magnitude and are of 10% of the total magnitude of AR ( $\sim 500 \text{ kgm}^{-1}\text{s}^{-1}$ ) (Figure 2). The variability  
297 in the magnitude of IVT300 in different products might lead to bias in the intensity, estimation of

298 precipitation and winds during landfall. Hence, we use ERA5 data as a standard dataset in our  
299 further analysis in the following sections.

### 300 **Spatio-temporal variability of IVT300**

301 The annual, WHY and SHY mean IVT computed using ERA5 data in IVT\_Upper (Figures  
302 S4a, S4d, S4g), IVT\_Middle (Figure S4b, S4e, S4h) and IVT\_Lower (Figure S4c, S4f, S4i) are  
303 shown in Supplementary Figure S4. Due to low saturated water vapour in the higher altitudes,  
304 IVT\_Upper in the North Atlantic has lower magnitude ( $20 \text{ kgm}^{-1}\text{s}^{-1}$ ) as compared to IVT\_Middle  
305 ( $>80 \text{ kgm}^{-1}\text{s}^{-1}$ ) and IVT\_Lower ( $70 \text{ kgm}^{-1}\text{s}^{-1}$ ) during all seasons. Though the magnitude is less,  
306 winds in the IVT\_Upper plays a key role in guiding these narrow filaments of ARs. As the  
307 IVT\_Middle (750-300 hPa) includes IVT\_Upper (500-300 hPa), the total IVT in the 750-500 hPa  
308 layer is  $60 \text{ kgm}^{-1}\text{s}^{-1}$ . When separating these pressure levels, IVT shows a dipole pattern with a low  
309 bellow  $20^\circ\text{N}$  over the northwestern African coast and a high in the central North Atlantic extending  
310 from  $30^\circ\text{N}$  to  $60^\circ\text{N}$ . The green rectangular box in Figure S4b shows the region with maximum IVT  
311 ( $30^\circ\text{N}$ - $60^\circ\text{N}$ ,  $80^\circ\text{W}$ - $0$ ). The magnitude of high in the dipole is further increased during SHY than  
312 other periods in all layers (Figure S4g-S4i). Similarly, the low has become further less during  
313 WHY (Figure S4d-S4f). Thus, IVT has maximum strength during SHY which could be due to  
314 increased evaporation over the warm waters in the North Atlantic. Figure 5 shows the strength of  
315 annual, SHY and WHY mean IVT in the central North Atlantic ( $30^\circ\text{N}$ - $60^\circ\text{N}$ ,  $80^\circ\text{W}$ - $0$ ) computed  
316 from ERA5 data using different reference pressure levels at the top (300 hPa, 500 hPa and 750  
317 hPa) with respect to 1000 hPa. No significant difference was seen between IVT500 and IVT300  
318 ( $\sim 12 \text{ kgm}^{-1}\text{s}^{-1}$ ) during the study period. But, IVT750 contributing  $\frac{3}{4}$  of the total strength of IVT300  
319 and IVT500. Thus, the strength of the IVT300 and IVT500 depends on the near-surface processes  
320 below 750 hPa. While there were no large changes in the strength of the IVT in the individual

321 layers with seasons; IVT in SHY has 3% higher magnitude, whereas IVT in WHY shows 3% lower  
322 magnitude compared to the annual mean (Figure 5). Hence, mean IVT is high in the below 500  
323 hPa of the atmosphere irrespective of the season. Thus, improved parameterization, in addition to  
324 accurate and high-resolution atmospheric data, at least up to 500 hPa would be handy in better  
325 estimating the strength of the IVT in the North Atlantic.

326

327 Furthermore, we show a Hovmöller diagram (Figure 6) of the monthly IVT300 in the  
328 central North Atlantic averaged between 30°N-60°N along 80°W-0 during 2014-2018 to study the  
329 seasonal variability of peak IVT300 in more detail. IVT300 peaks in the western Atlantic (along  
330 the east coast of North America) during summer months. Due to large temperature and pressure  
331 gradients from south to north coupled with extratropical cyclone season; high IVT300 has been  
332 shifting towards the eastern Atlantic in winter as marked with transparent arrows in Figure 6 and  
333 thus causing frequent ARs landfall over Western Europe during WHY. Yet, the extent, location  
334 and movement of the peak IVT300 were not constant and have large interannual variability with  
335 relatively low values during the spring season and hence the low AR activity during this time. This  
336 interannual and intraseasonal variability in IVT300 could be caused by the altering winds over this  
337 region. To study this further, we explored the decadal variability and trend in IVT300 and related  
338 atmospheric components in the following section.

### 339 **IVT300 decadal variability and trend**

340 It is evident that recent climate change cause global warming and alter the global water  
341 cycle. On this note, it important to look for changes in the IVT variability and trend during the past  
342 decades due to warming surface and enhanced evaporation as the changing Clausius-Clapeyron  
343 scaling factor  $\alpha(T)$  which could increase the total water vapour content in the individual

344 atmospheric layers. In Figure 7, we show the decadal trend and variability of IVT300 (daily  
345 anomaly). Similarly, IVT of different layers of the atmosphere and its dependency on the variable  
346 atmospheric parameters using ERA5 data is shown in Figure 8. For this purpose, we used the same  
347 region in the central North Atlantic (30°N-60°N, 80°W-0). Figure 8a shows an increasing annual  
348 trend of IVT300 anomaly (black line) in each decade over this region. IVT300 anomaly show  
349 significant seasonal and interannual variability. Though the overall trend shows an increasing  
350 IVT300 anomaly over this region with  $1063 \text{ kgm}^{-1}\text{yr}^{-1}$  in the study period, the decadal trend has  
351 seesaw oscillations. An annual IVT300 anomaly trend ( $199.1 \text{ kgm}^{-1}\text{yr}^{-1}$ ) in the first decade, i.e.  
352 1979-1988 (red) is dominated by the annual trend in the second decade (green) with an increase of  
353  $1591 \text{ kgm}^{-1}\text{yr}^{-1}$  (1989-1998). Similarly, a large increase in the annual IVT300 anomaly in the  
354 recent decade (purple) with  $4122 \text{ kgm}^{-1}\text{yr}^{-1}$  (2009-2018) dominates the previous decade (blue) with  
355 a moderate annual increase of  $42.52 \text{ kgm}^{-1}\text{yr}^{-1}$  (1999-2008).

356 This increasing annual IVT300 trend in each decade is in coherent with the increasing IVT  
357 below 750 hPa and IVT\_Lower (750-500 hPa) (Figure 8a). Particularly IVT750 has contributed  
358 more to the large increase in second (1989-1998) and fourth decades (2009-2018). As the IVT is  
359 proportional to Q, U and V; changes in these parameters would impact these trends. Thus, the large  
360 trend of IVT300 in the second decade is dominated by the availability of Q in the near-surface  
361 layer (1000-750 hPa) which has an annual increasing trend of  $2.5 \text{ gkg}^{-1}$  and is largest in all decades  
362 (Figure 8b). However, the negative trend in the zonal and meridional components of wind (Figures  
363 8c, 8d) in all layers during the same time, guides the total trend in the second decade. Though Q  
364 has a positive trend in the first and third decade, the negative trend in wind components during the  
365 same time in different layers caused the IVT annual trend to be moderate in these decades. On the  
366 other hand, the annual trend of both Q and wind components (U and V) were positive in the fourth

367 decade (Figure 8b-8d) and thus led to a strong increase in the annual IVT300 in all layers (Figure  
368 8c). Though the mean IVT flow is zonal, in the last two decades the meridional wind shows a  
369 positive trend (Figure 8c), which could be increasing the flow towards north and driving ARs  
370 poleward.

371         The spatial trend analysis significant at 95% during annual, WHY and SHY using daily  
372 IVT300 data from ERA5 is shown in Figure 9. While the annual trend shows a rapid increase  
373 ( $3000 \text{ kgm}^{-1}\text{yr}^{-1}$ ) of IVT300 at  $20^{\circ}\text{N}$  in the Atlantic and along the western Atlantic extended into  
374 central Atlantic with mean annual IVT300 increase of  $2000 \text{ kgm}^{-1}\text{yr}^{-1}$ , there was no significant  
375 increase in IVT300 over southwestern Europe during the study period (Figure 9c). There are  
376 seasonal differences, where both WHY and SHY show opposite spatial trends. IVT300 was  
377 increased in the central Atlantic and the southwestern United Kingdom during SHY, which could  
378 be triggered by the large IVT300 available over the western Atlantic during this time (Figure 9b,  
379 Figure 6). Though the WHY show opposite patterns with a negative trend in IVT300, the low is  
380 over the northern United Kingdom. There was a moderate increase in the IVT300 trend along  
381 southwestern Europe and the region below  $20^{\circ}\text{N}$  has a large positive trend during WHY (Figure  
382 9a). IVT300 has been increasing poleward in recent times with a strong positive trend along  $45^{\circ}\text{W}$   
383 during all seasons, which could lead to intense AR moving towards the north.

#### 384 **Categories and frequency of ARs over the North Atlantic**

385         The spatial variability of frequency of ARs over North Atlantic using different categories  
386 of IVT300 is shown in table 2. We distinguish the daily IVT300 based on Ralph et al., (2019) with  
387 some minor changes to the thresholds, but only using the magnitude of the intensity at each grid  
388 point or location in the selected region without considering the duration of the event. The spatial  
389 frequency has been computed using the percentage of the ratio of the number of days of IVT300

390 of the specific category to the total number of days in the study period (14610 days). Thus, cat 1  
391 events are more frequent in the North Atlantic which occurs at 50% of the time (Figure 10a) along  
392 the southwest coast of Europe and in the central Atlantic. Other category (cat 2, cat 3 and cat 4)  
393 events are less frequent (<15%) over the Euro-Atlantic region (Figure 10b-10d). The humidity  
394 source of this intense IVT300 is along the western Atlantic and a few events are reaching the west  
395 coast of Europe. Thus, the frequency of intense ARs over Europe is less with cat 2, IVT300 being  
396 at 8%, cat 3 and cat 4 are at below 1% of the time. Nonetheless, the rare intense events which occur  
397 at less than 1% of the time potentially cause large damage over coastal areas. To investigate the  
398 same along Western Europe, we draw the frequency histogram (Figure 11a) and compute the  
399 probability density function (Figure 11b) along 11°W as a gateway to Western Europe. This is  
400 different compared to Lavers et al., (2013) who considered 10°W as the reference longitude which  
401 intersects with some parts of the land over the United Kingdom. Assuming 11°W and 35°N-70°N  
402 would eliminate the IVT300 interaction with land.

403 While most of the IVT300 values along the west coast during the study period are below  
404  $300 \text{ kgm}^{-1}\text{s}^{-1}$  (Figure 11a), the values reaching  $800 \text{ kgm}^{-1}\text{s}^{-1}$  in a few instances could lead to  
405 extreme ARs. Similarly, the probability density function computed along the same boundary  
406 (Figure 11b) shows the IVT300 could reach up to  $1400 \text{ kgm}^{-1}\text{s}^{-1}$  and cat 1 IVT300 has the higher  
407 probability of occurrence ( $>0.02$ ) over Western Europe than other categories. The decadal analysis  
408 along the same longitude (Figure 12) shows an increasing extreme IVT300 values and their  
409 poleward shift in recent decades. All categories show peak frequency between 40°N-60°N and  
410 there is no explicit decadal variability of cat 1 IVT300 along 11°W (Figure 12a). But cat 2 (Figure  
411 12b,12c) shows low frequency during the first (black) and third decades between 40°N-60°N  
412 (green). On the other hand, the frequency of cat 3 and cat 4 IVT300 has been increasing with time

413 (Figure 12d) and there is poleward movement of  $\sim 5^\circ$  towards north and crossing  $60^\circ\text{N}$ . The changes  
414 in the atmospheric state and the synoptic condition in recent decades could be causing the poleward  
415 movement of the intense IVT300. Hence, in the following section, we study the state of the  
416 atmosphere during the occurrence of IVT300 over Western Europe.

### 417 **Atmospheric state and synoptic conditions**

418 The Scandinavian blocking including phases of the NAO dominates weather patterns over  
419 Europe and Scandinavia through the impact on precipitation and temperature (Madonna et al.,  
420 2017). While these patterns are persistent in the North Atlantic-European sector irrespective of the  
421 seasons, mostly these patterns control the wintertime weather regimes (Dawson et al., 2012;  
422 Hannachi et al., 2017). On the other hand, Western Europe receives more frequent intense IVT300  
423 (ARs) in wintertime than in any other season. To study the atmospheric and synoptic conditions  
424 while IVT300 occurrence and landfall along Western Europe, we study the composite of 500 hPa  
425 geopotential (GP) (Figure 13) and surface latent heat flux (SLHF) (Figure 14) anomalies following  
426 Lavers et al., (2013) along  $11^\circ\text{W}$  using  $5^\circ$  latitude bins spanning  $35^\circ\text{N}$ - $70^\circ\text{N}$  (Figure S5). Contrary  
427 to Lavers et al. (2013), who used only 10 intense ARs, we computed GP and SLHF anomaly  
428 composites with all instances (days) where IVT300 greater than  $200 \text{ kgm}^{-1}\text{s}^{-1}$  in these latitude bins.  
429 Initially, we computed these daily GP and SLHF anomalies with respect to the same time (day)  
430 period during 1979-2018. Then, these anomalies were picked with respect to time and location of  
431 the occurrence of IVT300 greater than  $200 \text{ kgm}^{-1}\text{s}^{-1}$  within selected bins and the composite mean  
432 anomaly was calculated for each latitude bin.

433 GP shows a tripole pattern with positive anomalies over south of the Iberian Peninsula  
434 (Figure 13a and 13b); Iceland and Greenland, and negative anomalies extend from Britain to the  
435 Iberian Peninsula. This is also termed as an Atlantic ridge regime with blocking mainly offshore

436 of the Iberian Peninsula due to Iberian wave breaking (Davini et al., 2014) or southwest European  
437 blocking (Woollings et al., 2010) leading to the southward occurring ARs (35°N-45°N). The  
438 Greenland anticyclone regime occurs mainly over Greenland resembling the negative phase of the  
439 NAO. This negative NAO arrangement would block the flow over northern Europe and the North  
440 Atlantic storm track and related heavy precipitation and thus impacts southern Europe (Pinto and  
441 Raible, 2012). The zonal regime with very little blocking resembling the positive phase of the  
442 NAO. In a positive NAO phase, negative GP anomalies (Figure 13c and 13d) in the 45°N-55°N  
443 latitude band favours occurrence of frequent IVT300 within the extratropical cyclones causing  
444 rainfall over northern France, through the western British Isles to Norway. A Scandinavian  
445 blocking regime is associated with blocking mainly over the European continent and Scandinavia.  
446 The occurrence of IVT300 (ARs) and their associated precipitation in the north between 55°N-  
447 70°N is related to Scandinavian blocking with the dipole of positive anomalies near the British  
448 Isles and negative anomalies over Greenland and Iceland (Figure 13e-13g). Although both NAO  
449 and Scandinavian patterns have strong relation with IVT300 occurrence in Europe, it is not obvious  
450 that each IVT300 (AR) landfall would follow the same synoptic weather patterns as the spatial  
451 pattern of the atmospheric state would vary significantly with time over a region.

452         Southernmost IVT300 events are drawing water vapour from both western and eastern  
453 North Atlantic as SLHF anomalies show a dipole pattern with positive anomalies on either side  
454 (Figure 14a, 14b). Thus, these regions act as a major source to moisture entraining into ARs and  
455 impact the intensity of IVT300. The north-central Atlantic is the source of moisture for the IVT300  
456 in the 45°N-55°N latitude band (Figure 14c, 14d). Further, a dipole pattern with positive SLHF  
457 anomaly in the west and negative in the east fueling IVT300 in the far north. Though the positive  
458 anomalies over the North Atlantic could lead to intensifying IVT300 in the north, the cold sea

459 surface and associated negative SLHF anomalies over the Scandinavia could control the total  
460 moisture flux into the IVT300 and hence the intensity of ARs over this region.

## 461 **Conclusions**

462 We have studied the spatiotemporal variability of water vapour transport (IVT and IWV)  
463 as a proxy to ARs in the Euro-Atlantic basin using six-hourly ERA5 data and evaluated five other  
464 reanalysis data sets available from NOAA, NASA, ECMWF and NCEP during 1979-2018 with  
465 ERA5. We use IVT and IWV methods to map the water vapour transport in different atmospheric  
466 layers, the North Atlantic and normalized with temperature to study the water vapour variability  
467 with temperature. Both IVT and nIVT proved to accurate enough to map ARs. Though the IVT  
468 shows seasonal and semi-annual variability; the mean annual intensity of IVT300 is  $300 \text{ kgm}^{-1}\text{s}^{-1}$ ,  
469 and the standard deviation is at 60% of the intensity in the North Atlantic. On the other hand, both  
470 these values vary in different reanalysis products, with recently released ERA5 showing lower  
471 climatology and standard deviation whereas ERA-Interim has higher values compared to other  
472 reanalysis datasets. However, the average bias in other datasets is around  $60 \text{ kgm}^{-1}\text{s}^{-1}$  as compared  
473 to ERA5 which amounts to 22% of the total observed IVT flux. The bias in the magnitude of IVT  
474 in different layers is directly proportional to the bias in the Q, U and V of the respective layers.  
475 Both the accuracy and magnitude of atmospheric variables at different pressure levels (Q, U and  
476 V) in mapping ARs are highly dependent on the resolution of the data obtained. Many of the  
477 existing algorithms and mapping techniques are using atmospheric data from satellites and  
478 numerical models. Numerical models have limitation in integrating the discretized version of the  
479 Navier-Stokes equations. Due to uncertainty in initial conditions, numerical approximation, and  
480 model deficiencies, the error increases non-linearly and thus have decreasing forecast skill in  
481 simulating the state of the atmosphere with a good lead time (e.g. Lorenz, 1963). As the filament

482 structures move with time, and the Eulerian method used to map filaments make it hard to use  
483 observations. On the other hand, most of the ARs, originate from the large open oceans through  
484 both local evaporation and remote moisture flux convergence. Land-based stations could be handy  
485 in measuring the atmospheric parameters while the AR approach in land and landfall. Data  
486 obtained from both satellites and statistical methods have limitations in forecasting the landfall  
487 and intensity of ARs well in advance. In recent times machine learning techniques (Chapman et  
488 al., 2019; Kashinath et al., 2020) have evolved as other alternatives. However, the mean error in  
489 estimating the intensity of ARs through IVT is around 40-60  $\text{kgm}^{-1}\text{s}^{-1}$  using different sources of  
490 data including data from reanalysis and amounts to 22% of mean observed flux (Chapman et al.,  
491 2019, Lavers et al., 2018).

492 While most of the water vapour flux located below 500 hPa due to rapidly decreasing  
493 saturated moisture flux with height, the upper layer winds are key to transport the flux poleward.  
494 Hence, the accurate and high-resolution atmospheric parameters at least up to 500 hPa could  
495 improve the detection and tracking of ARs in the North Atlantic. On the other hand, the variability  
496 and trend of Q, U and V below 750 hPa guide the strength of the total column IVT. Thus, Q, U,  
497 and V below 750 hPa control the magnitude of IVT in the North Atlantic which shows an  
498 increasing decadal trend with seesaw decadal variability. The IVT in the North Atlantic shows  
499 interannual variability with the zonal movement of peak values from the western Atlantic in  
500 summer to the eastern Atlantic in winter. However, the strength of the IVT in the Atlantic is 3%  
501 higher in summer as compared to annual mean due to strong evaporation from the warm ocean  
502 than 3% low in winter. While the semi-annual spatial trend of IVT300 shows an opposite pattern,  
503 the annual trend of IVT300 shows an increasing water vapour flux over the western Atlantic with  
504 a poleward movement of this flux during the last decades. Thus, the higher latitudes encountering

505 intense ARs in recent times. Though the category 1 IVT300 are more frequent (50%) in the North  
506 Atlantic, particularly over 40°N-60°N, the rarely occurring (15%) higher category events could  
507 cause extreme precipitation, flooding and winds over Western Europe. The atmospheric state and  
508 synoptic weather guided by Scandinavian blocking and both phases of NAO set the landfall  
509 location of ARs along Western Europe.

510         There are several questions still open for the future work. We aimed at studying the impact  
511 of climate indices such as El Niño-Southern Oscillation (ENSO), Atlantic multidecadal oscillation,  
512 Atlantic zonal mode variability and changing synoptic circulation patterns on the intensity and  
513 frequency of ARs in the North Atlantic and the Western Europe. Furthermore, we will study the  
514 influence of oceanic parameters and the subtropical convection over the source regions in open  
515 oceans to understand the rapid enhancement of IVT300. Looking at the surface and sub-surface  
516 oceanic parameters in the North Atlantic Ocean would be handy to understand the strength of the  
517 IVT300 over the region. Also, changes in the surface temperatures over the Gulf current and  
518 subtropical gyre in the North Atlantic Ocean might give some insights on ARs variability. Changes  
519 in the coastal sea level and subsurface processes are also key to understand while studying impacts  
520 of land falling ARs. Similarly, we will investigate the implications of recent poleward shift in the  
521 location of landfall ARs in the North Atlantic on changes in Greenland and Arctic mass balance  
522 which is out of scope of present work.

523

#### 524 **Data availability**

525 All data used in the study are freely available online from the corresponding data sources cited in  
526 the article. However, data that support the findings of this study are available on request from the  
527 corresponding author.

528

529 **Code availability**

530 All codes used in this study are available on request from the corresponding author.

531

532 **Acknowledgement**

533 Authors thank NOAA Earth System Research Laboratories (ESRL), the European Centre for  
534 Medium-Range Weather Forecasts (ECMWF), the National Aeronautics and Space  
535 Administration (NASA), and the National Centers for Environmental Prediction (NCEP) for  
536 providing reanalysis datasets. We acknowledge Pyferret software from the NOAA/PMEL. We  
537 acknowledge the Department of Earth Sciences, Uppsala University and the Swedish Research  
538 Council (VR) nr 2017-03988 for supporting this study. Thanks to Paulo De Luca, Department of  
539 Water and Climate Risk, Vrije Universiteit, Amsterdam for useful comments to improve the  
540 manuscript.

541

542 **References**

543 Blamey, R. C., A. M. Ramos, R. M. Trigo, R. Tomé, and C. J. C. Reason. "The influence of  
544 atmospheric rivers over the South Atlantic on winter rainfall in South Africa." *Journal of*  
545 *Hydrometeorology* 19, no. 1 (2018): 127-142.

546 Champion, Adrian J., Richard P. Allan, and David A. Lavers. "Atmospheric rivers do not  
547 explain UK summer extreme rainfall." *Journal of Geophysical Research: Atmospheres* 120,  
548 no. 14 (2015): 6731-6741.

549 Chapman, W. E., A. C. Subramanian, L. Delle Monache, S. P. Xie, and F. M. Ralph.  
550 "Improving Atmospheric River Forecasts With Machine Learning." *Geophysical Research*  
551 *Letters* 46, no. 17-18 (2019): 10627-10635.

552 Cheng, Brian S., Andrew L. Chang, Anna Deck, and Matthew C. Ferner. "Atmospheric rivers  
553 and the mass mortality of wild oysters: insight into an extreme future?." *Proceedings of the*  
554 *Royal Society B: Biological Sciences* 283, no. 1844 (2016): 20161462.

555 Compo, G.P., J.S. Whitaker, P.D. Sardeshmukh, N. Matsui, R.J. Allan, X. Yin, B.E. Gleason,  
556 R.S. Vose, G. Rutledge, P. Bessemoulin, S. Brönnimann, M. Brunet, R.I. Crouthamel, A.N.  
557 Grant, P.Y. Groisman, P.D. Jones, M. Kruk, A.C. Kruger, G.J. Marshall, M. Maugeri, H.Y.  
558 Mok, Ø. Nordli, T.F. Ross, R.M. Trigo, X.L. Wang, S.D. Woodruff, and S.J. Worley, 2011:  
559 The Twentieth Century Reanalysis Project. *Quarterly J. Roy. Meteorol. Soc.*, 137, 1-28.  
560 <http://dx.doi.org/10.1002/qj.776>

561 Cordeira, Jason M., Jonathan Stock, Michael D. Dettinger, Allison M. Young, Julie F.  
562 Kalansky, and F. Martin Ralph. "A 142-year climatology of northern California landslides and  
563 atmospheric rivers." *Bulletin of the American Meteorological Society* 100, no. 8 (2019): 1499-  
564 1509.

565 Dawson A, Palmer TN, Corti S. 2012. Simulating regime structures in weather and climate  
566 prediction models. *Geophys. Res. Lett.* 39: L21805.

567 De Luca, P., Hillier, J. K., Wilby, R. L., Quinn, N. W., & Harrigan, S. (2017). Extreme multi-  
568 basin flooding linked with extra-tropical cyclones. *Environmental Research Letters*, 12(11),  
569 114009.

570 Dee, D. P., and 35 co-authors, 2011: The ERA-Interim reanalysis: Configuration and  
571 performance of the data assimilation system. *Quart. J. R. Meteorol. Soc.*, 137, 553-597. DOI:  
572 10.1002/qj.828.

573 Dettinger, M. (2011). Climate change, atmospheric rivers, and floods in California—a  
574 multimodel analysis of storm frequency and magnitude changes 1. *JAWRA Journal of the*  
575 *American Water Resources Association*, 47(3), 514-523.

576 Dettinger, M. D., F. M. Ralph, T. Das, P. J. Neiman, and D. R. Cayan (2011), Atmospheric  
577 rivers, floods and the water resources of California, *Water*, 3, 445–478,  
578 doi:10.3390/w3020445.

579 Dettinger, Michael D., Fred Martin Ralph, Tapash Das, Paul J. Neiman, and Daniel R. Cayan.  
580 "Atmospheric rivers, floods and the water resources of California." *Water* 3, no. 2 (2011): 445-  
581 478.

582 Fish, Meredith A., Anna M. Wilson, and F. Martin Ralph. "Atmospheric River Families:  
583 Definition and Associated Synoptic Conditions." *Journal of Hydrometeorology* 20, no. 10  
584 (2019): 2091-2108.

585 Florsheim, Joan L., and Michael D. Dettinger. "Promoting atmospheric-river and snowmelt-  
586 fueled biogeomorphic processes by restoring river-floodplain connectivity in California's  
587 Central Valley." In *Geomorphic approaches to integrated floodplain management of lowland*  
588 *fluvial systems in North America and Europe*, pp. 119-141. Springer, New York, NY, 2015.

589 Gao, Yang, Jian Lu, and L. Ruby Leung. "Uncertainties in projecting future changes in  
590 atmospheric rivers and their impacts on heavy precipitation over Europe." *Journal of Climate*  
591 29, no. 18 (2016): 6711-6726.

592 Gao, Yang, Jian Lu, and L. Ruby Leung. "Uncertainties in projecting future changes in  
593 atmospheric rivers and their impacts on heavy precipitation over Europe." *Journal of Climate*  
594 29, no. 18 (2016): 6711-6726.

595 Gelaro, Ronald, Will McCarty, Max J. Suárez, Ricardo Todling, Andrea Molod, Lawrence  
596 Takacs, Cynthia A. Randles et al. "The modern-era retrospective analysis for research and  
597 applications, version 2 (MERRA-2)." *Journal of Climate* 30, no. 14 (2017): 5419-5454.

598 Gimeno, Luis, Andreas Stohl, Ricardo M. Trigo, Francina Dominguez, Kei Yoshimura, Lisan  
599 Yu, Anita Drumond, Ana María Durán-Quesada, and Raquel Nieto. "Oceanic and terrestrial  
600 sources of continental precipitation." *Reviews of Geophysics* 50, no. 4 (2012).

601 Gimeno, Luis, Raquel Nieto, Marta Vázquez, and David A. Lavers. "Atmospheric rivers: A  
602 mini-review." *Frontiers in Earth Science* 2 (2014).

603 Gimeno, Luis. "Grand challenges in atmospheric science." *Frontiers in Earth Science* 1 (2013).

604 Gonzales, K. R., Swain, D. L., Nardi, K. M., Barnes, E. A., & Diffenbaugh, N. S. (2019).  
605 Recent warming of landfalling atmospheric rivers along the west coast of the United States.  
606 *Journal of Geophysical Research: Atmospheres*, 124(13), 6810-6826.

607 Gorodetskaya, Irina V., Maria Tsukernik, Kim Claes, Martin F. Ralph, William D. Neff, and  
608 Nicole PM Van Lipzig. "The role of atmospheric rivers in anomalous snow accumulation in  
609 East Antarctica." *Geophysical Research Letters* 41, no. 17 (2014): 6199-6206.

610 Guan, Bin, and Duane E. Waliser. "Atmospheric rivers in 20 year weather and climate  
611 simulations: A multimodel, global evaluation." *Journal of Geophysical Research: Atmospheres*  
612 122, no. 11 (2017): 5556-5581.

613 Guan, Bin, and Duane E. Waliser. "Detection of atmospheric rivers: Evaluation and application  
614 of an algorithm for global studies." *Journal of Geophysical Research: Atmospheres* 120, no.  
615 24 (2015): 12514-12535.

616 Guan, Bin, Noah P. Molotch, Duane E. Waliser, Eric J. Fetzer, and Paul J. Neiman. "Extreme  
617 snowfall events linked to atmospheric rivers and surface air temperature via satellite  
618 measurements." *Geophysical Research Letters* 37, no. 20 (2010).

619 Hack, James J., Julie M. Caron, Stephen G. Yeager, Keith W. Oleson, Marika M. Holland,  
620 John E. Truesdale, and Philip J. Rasch. "Simulation of the global hydrological cycle in the  
621 CCSM Community Atmosphere Model version 3 (CAM3): Mean features." *Journal of climate*  
622 19, no. 11 (2006): 2199-2221.

623 Hannachi A, Straus DM, Franzke CLE, Corti S, Woollings T. 2017. Low-frequency  
624 nonlinearity and regime behavior in the Northern Hemisphere extratropical atmosphere. *Rev.*  
625 *Geophys.* 55: 199-234.

626 Hersbach, H et al., Copernicus Climate Change Service (C3S) (2017): ERA5: Fifth generation  
627 of ECMWF atmospheric reanalyses of the global climate. Copernicus Climate Change Service  
628 Climate Data Store (CDS)

629 Huning, Laurie S., Steven A. Margulis, Bin Guan, Duane E. Waliser, and Paul J. Neiman.  
630 "Implications of detection methods on characterizing atmospheric river contribution to  
631 seasonal snowfall across Sierra Nevada, USA." *Geophysical Research Letters* 44, no. 20  
632 (2017): 10-445.

633 Kamae, Youichi, Wei Mei, and Shang-Ping Xie. "Climatological relationship between warm  
634 season atmospheric rivers and heavy rainfall over East Asia." *Journal of the Meteorological*  
635 *Society of Japan. Ser. II* (2017).

636 Kanamitsu, Masao, Wesley Ebisuzaki, Jack Woollen, Shi-Keng Yang, J. J. Hnilo, M. Fiorino,  
637 and G. L. Potter. "Ncep–doe amip-ii reanalysis (r-2)." *Bulletin of the American Meteorological*  
638 *Society* 83, no. 11 (2002): 1631-1644.

639 Kashinath, K., Mudigonda, M., Kim, S., Kapp-Schwoerer, L., Graubner, A., Karaismailoglu,  
640 E., ... & Lewis, C. (2020). ClimateNet: an expert-labelled open dataset and Deep Learning  
641 architecture for enabling high-precision analyses of extreme weather. *Geoscientific Model*  
642 *Development Discussions*, 1-28.

643 Kaye L. Brubaker, Dara Entekhabi, and Peter S. Eagleson. Atmospheric water vapor transport  
644 and continental hydrology over the Americas. Technical Report 3-4, 1994.

645 Khouakhi, A., and G. Villarini. "On the relationship between atmospheric rivers and high sea  
646 water levels along the US West Coast." *Geophysical Research Letters* 43, no. 16 (2016): 8815-  
647 8822.

648 Komatsu, Kensuke K., Vladimir A. Alexeev, Irina A. Repina, and Yoshihiro Tachibana.  
649 "Poleward upgliding Siberian atmospheric rivers over sea ice heat up Arctic upper air."  
650 *Scientific reports* 8, no. 1 (2018): 1-15.

651 Kundzewicz, Zbigniew W., Maciej Radziejewski, and Iwona Pinskiwar. "Precipitation  
652 extremes in the changing climate of Europe." *Climate Research* 31, no. 1 (2006): 51-58.

653 Lavers, D. A., & Villarini, G. (2013). Atmospheric rivers and flooding over the central United  
654 States. *Journal of Climate*, 26(20), 7829-7836.

655 Lavers, D. A., & Villarini, G. (2013). The nexus between atmospheric rivers and extreme  
656 precipitation across Europe. *Geophysical Research Letters*, 40(12), 3259-3264.

657 Lavers, David A., and Gabriele Villarini. "The contribution of atmospheric rivers to  
658 precipitation in Europe and the United States." *Journal of Hydrology* 522 (2015): 382-390.

659 Lavers, David A., Florian Pappenberger, David S. Richardson, and Ervin Zsoter. "ECMWF  
660 Extreme Forecast Index for water vapor transport: A forecast tool for atmospheric rivers and  
661 extreme precipitation." *Geophysical Research Letters* 43, no. 22 (2016): 11-852.

662 Lavers, David A., Gabriele Villarini, Richard P. Allan, Eric F. Wood, and Andrew J. Wade.  
663 "The detection of atmospheric rivers in atmospheric reanalyses and their links to British winter  
664 floods and the large-scale climatic circulation." *Journal of Geophysical Research:*  
665 *Atmospheres* 117, no. D20 (2012).

666 Lavers, David A., Mark J. Rodwell, David S. Richardson, F. Martin Ralph, James D. Doyle,  
667 Carolyn A. Reynolds, Vijay Tallapragada, and Florian Pappenberger. "The gauging and  
668 modeling of rivers in the sky." *Geophysical Research Letters* 45, no. 15 (2018): 7828-7834.

669 Lavers, David A., Richard P. Allan, Eric F. Wood, Gabriele Villarini, David J. Brayshaw, and  
670 Andrew J. Wade. "Winter floods in Britain are connected to atmospheric rivers." *Geophysical*  
671 *Research Letters* 38, no. 23 (2011).

672 Lavers, David A., Richard P. Allan, Eric F. Wood, Gabriele Villarini, David J. Brayshaw, and  
673 Andrew J. Wade. "Winter floods in Britain are connected to atmospheric rivers." *Geophysical*  
674 *Research Letters* 38, no. 23 (2011).

675 Leung, L. Ruby, and Yun Qian. "Atmospheric rivers induced heavy precipitation and flooding  
676 in the western US simulated by the WRF regional climate model." *Geophysical Research*  
677 *Letters* 36, no. 3 (2009).

678 Madonna, E., Li, C., Grams, C. M., & Woollings, T. (2017). The link between eddy-driven jet  
679 variability and weather regimes in the North Atlantic-European sector. *Quarterly Journal of*  
680 *the Royal Meteorological Society*, 143(708), 2960-2972.

681 Mattingly, K. S., T. L. Mote, and Xavier Fettweis. "Atmospheric river impacts on Greenland  
682 Ice Sheet surface mass balance." *Journal of Geophysical Research: Atmospheres* 123, no. 16  
683 (2018): 8538-8560.

684 Millán, Millán M. "Extreme hydrometeorological events and climate change predictions in  
685 Europe." *Journal of Hydrology* 518 (2014): 206-224.

686 Nash, Deanna, Duane Waliser, Bin Guan, Hengchun Ye, and F. Martin Ralph. "The role of  
687 atmospheric rivers in extratropical and polar hydroclimate." *Journal of Geophysical Research:*  
688 *Atmospheres* 123, no. 13 (2018): 6804-6821.

689 Neff, William. "Atmospheric rivers melt Greenland." *Nature Climate Change* 8, no. 10 (2018):  
690 857-858.

691 Neiman, Paul J., F. Martin Ralph, Gary A. Wick, Jessica D. Lundquist, and Michael D.  
692 Dettinger. "Meteorological characteristics and overland precipitation impacts of atmospheric  
693 rivers affecting the West Coast of North America based on eight years of SSM/I satellite  
694 observations." *Journal of Hydrometeorology* 9, no. 1 (2008a): 22-47.

695 Neiman, Paul J., Lawrence J. Schick, F. Martin Ralph, Mimi Hughes, and Gary A. Wick.  
696 "Flooding in western Washington: The connection to atmospheric rivers." *Journal of*  
697 *Hydrometeorology* 12, no. 6 (2011): 1337-1358.

698 Pasquier, J. T., Stephan Pfahl, and Christian M. Grams. "Modulation of atmospheric river  
699 occurrence and associated precipitation extremes in the North Atlantic Region by European  
700 weather regimes." *Geophysical Research Letters* 46, no. 2 (2019): 1014-1023.

701 Payne, Ashley E., Marie-Estelle Demory, L. Ruby Leung, Alexandre M. Ramos, Christine A.  
702 Shields, Jonathan J. Rutz, Nicholas Siler, Gabriele Villarini, Alex Hall, and F. Martin Ralph.

703 "Responses and impacts of atmospheric rivers to climate change." *Nature Reviews Earth &*  
704 *Environment* (2020): 1-15.

705 Pinto, J. G., and C. C. Raible (2012), Past and recent changes in the North Atlantic oscillation,  
706 *WIREs Clim. Change*, 3,79–90, doi:10.1002/ wcc.150.

707 Pinto, Joaquim G., Nina Bellenbaum, Melanie K. Karremann, and Paul M. Della-Marta. "Serial  
708 clustering of extratropical cyclones over the North Atlantic and Europe under recent and future  
709 climate conditions." *Journal of geophysical research: Atmospheres* 118, no. 22 (2013): 12-476.

710 Ralph, F. M., & Dettinger, M. D. (2011). Storms, floods, and the science of atmospheric rivers.  
711 *Eos, Transactions American Geophysical Union*, 92(32), 265-266.

712 Ralph, F. Martin, Jonathan J. Rutz, Jason M. Cordeira, Michael Dettinger, Michael Anderson,  
713 David Reynolds, Lawrence J. Schick, and Chris Smallcomb. "A scale to characterize the  
714 strength and impacts of atmospheric rivers." *Bulletin of the American Meteorological Society*  
715 100, no. 2 (2019): 269-289.

716 Ramos, Alexandre M., Ross C. Blamey, Iago Algarra, Raquel Nieto, Luis Gimeno, Ricardo  
717 Tomé, Chris JC Reason, and Ricardo M. Trigo. "From Amazonia to southern Africa:  
718 atmospheric moisture transport through low level jets and atmospheric rivers." *Ann. NY Acad.*  
719 *Sci* 1436 (2018): 217-230.

720 Saha, Suranjana, Shrinivas Moorthi, Xingren Wu, Jiande Wang, Sudhir Nadiga, Patrick Tripp,  
721 David Behringer et al. "The NCEP climate forecast system version 2." *Journal of climate* 27,  
722 no. 6 (2014): 2185-2208.

723 Schneider, Edwin K., Ben P. Kirtman, and Richard S. Lindzen. "Tropospheric water vapor and  
724 climate sensitivity." *Journal of the atmospheric sciences* 56, no. 11 (1999): 1649-1658.

725 Thapa, Kritika, Theodore A. Endreny, and Craig R. Ferguson. "Atmospheric rivers carry  
726 nonmonsoon extreme precipitation into Nepal." *Journal of Geophysical Research:  
727 Atmospheres* 123, no. 11 (2018): 5901-5912.

728 Thapa, Kritika, Theodore A. Endreny, and Craig R. Ferguson. "Atmospheric rivers carry non  
729 monsoon extreme precipitation into Nepal." *Journal of Geophysical Research: Atmospheres*  
730 123, no. 11 (2018): 5901-5912.

731 Trenberth, Kevin E. "Changes in precipitation with climate change." *Climate Research* 47, no.  
732 1-2 (2011): 123-138.

733 Van den Besselaar, E. J. M., A. M. G. Klein Tank, and T. A. Buishand. "Trends in European  
734 precipitation extremes over 1951–2010." *International Journal of Climatology* 33, no. 12  
735 (2013): 2682-2689.

736 Waliser, Duane, and Bin Guan. "Extreme winds and precipitation during landfall of  
737 atmospheric rivers." *Nature Geoscience* 10, no. 3 (2017): 179-183.

738 Yang, Yan, Tongtiegang Zhao, Guangheng Ni, and Ting Sun. "Atmospheric rivers over the  
739 Bay of Bengal lead to northern Indian extreme rainfall." *International Journal of Climatology*  
740 38, no. 2 (2018): 1010-1021.

741 Yang, Yan, Tongtiegang Zhao, Guangheng Ni, and Ting Sun. "Atmospheric rivers over the  
742 Bay of Bengal lead to northern Indian extreme rainfall." *International Journal of Climatology*  
743 38, no. 2 (2018): 1010-1021.

744 Zhu, Yong, and Reginald E. Newell. "A proposed algorithm for moisture fluxes from  
745 atmospheric rivers." *Monthly weather review* 126, no. 3 (1998): 725-735.

746 Zhu, Yong, and Reginald E. Newell. "A proposed algorithm for moisture fluxes from  
747 atmospheric rivers." *Monthly weather review* 126, no. 3 (1998): 725-735.

748 Zhu, Yong, and Reginald E. Newell. "Atmospheric rivers and bombs." *Geophysical Research*  
 749 *Letters* 21, no. 18 (1994): 1999-2002.

750

751 **Tables:**

752 Table 1: Details of reanalysis datasets used in the present study

Dataset	Source	Availability	Temporal Resolution	Spatial Resolution	Reference
20th Century Reanalysis (20CR-V2)	ESRL: PSD/NOAA	1851-2014	6 hourly	2 x 2 x 24, 1000 - 10 hPa	Compo et al., (2011)
ERA-Interim	ECMWF	1979-2018	6 hourly	0.75 x 0.75 x 60, 1000 - 0.1 hPa	Dee et al., (2011)
ERA5	ECMWF	1979-present	6 hourly	0.25 x 0.25 x 37 1000 - 1 hPa	Hersbach, H et al., (2017)
Modern-Era Retrospective analysis for Research and	Global Modelling and Assimilation Office	1980-present	6 hourly	0.5 x 0.625 x 42 1000 - 1 hPa	Gelaro et al., (2017)

Applications (MERRA-2)	(NASA)				
Climate Forecast System Reanalysis (CFSR-v2)	National Centers for Environmental Prediction (NCEP)	1979-present	6 hourly	38 x 64 km, 1000- 0.266 hPa	Saha et al., (2014)
NCEP-NCAR Reanalysis - v2	NCEP-NCAR	1979-present	6 hourly	2.5 x 2.5 x 28 1000 - 3 hPa	Kanamitsu et al., (2002)

753

754

Table 2: Categories of IVT300 based on intensity

S. No	Category	Threshold ( $\text{kgm}^{-1}\text{s}^{-1}$ )
1	Cat 1	$200 \leq \text{IVT300} < 500$
2	Cat 2	$500 \leq \text{IVT300} < 750$
3	Cat 3	$750 \leq \text{IVT300} < 1000$
4	Cat 4	$\text{IVT300} \geq 1000$

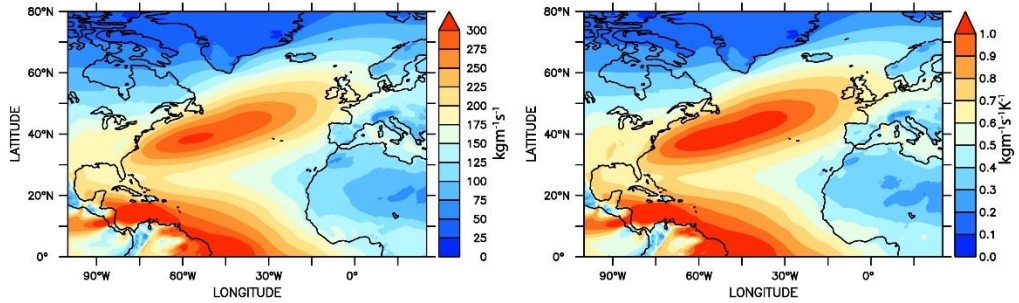
755

756

757

758 **Figures:**

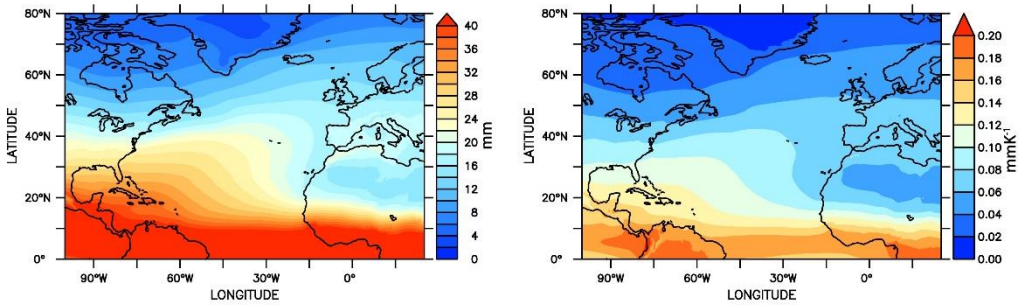
759



760

(a)IVT300 Climatology

(b)nIVT300 Climatology



761

(c)IWV300 Climatology

(d)nIWV300 Climatology

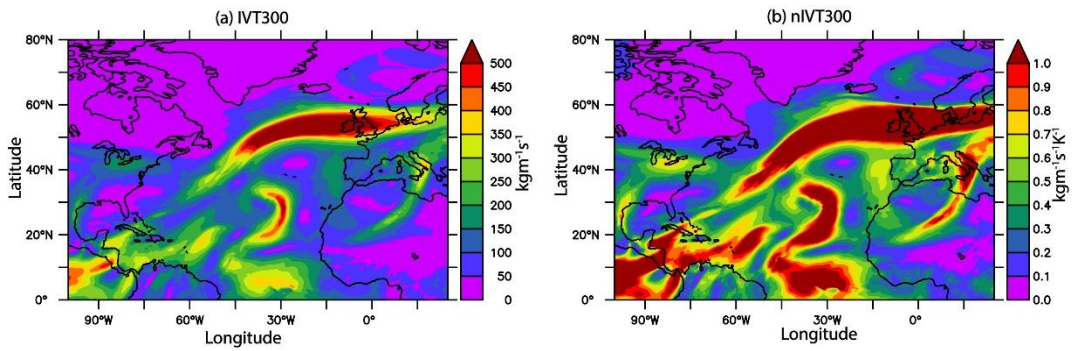
762 Figure 1: Climatology of ARs computed from daily ERA5 data using four different methods in

763

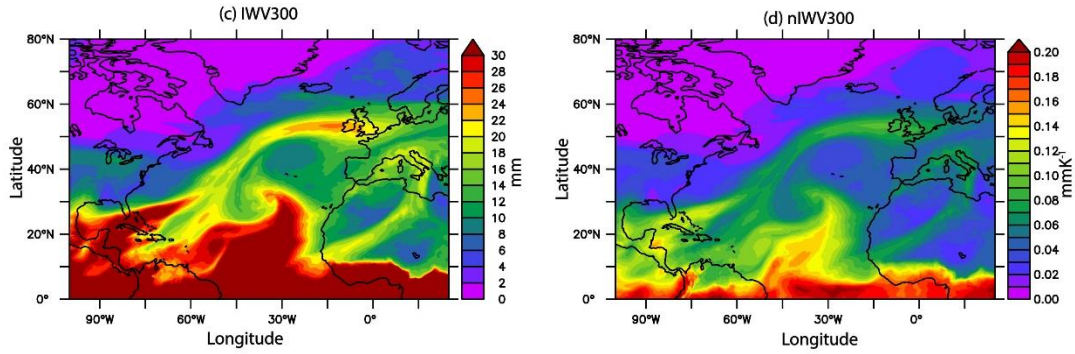
the North Atlantic

764

765



766



767

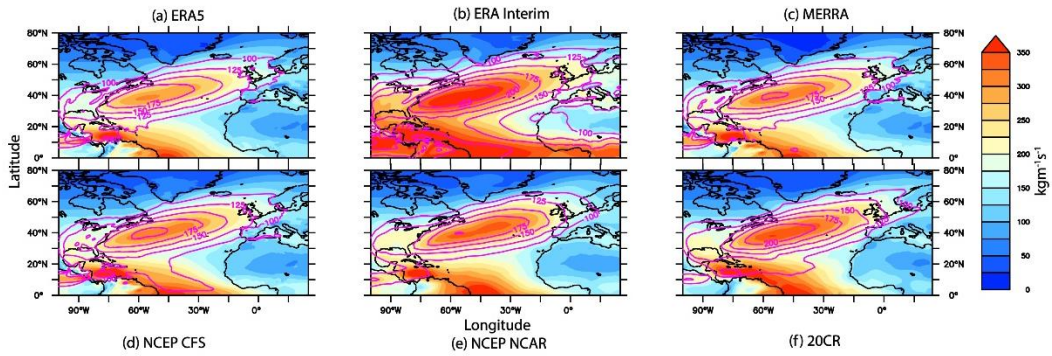
768

Figure 2: AR event on 2002 March 06 mapped using four different methods in the North

769

Atlantic using ERA5 data.

770



771

772

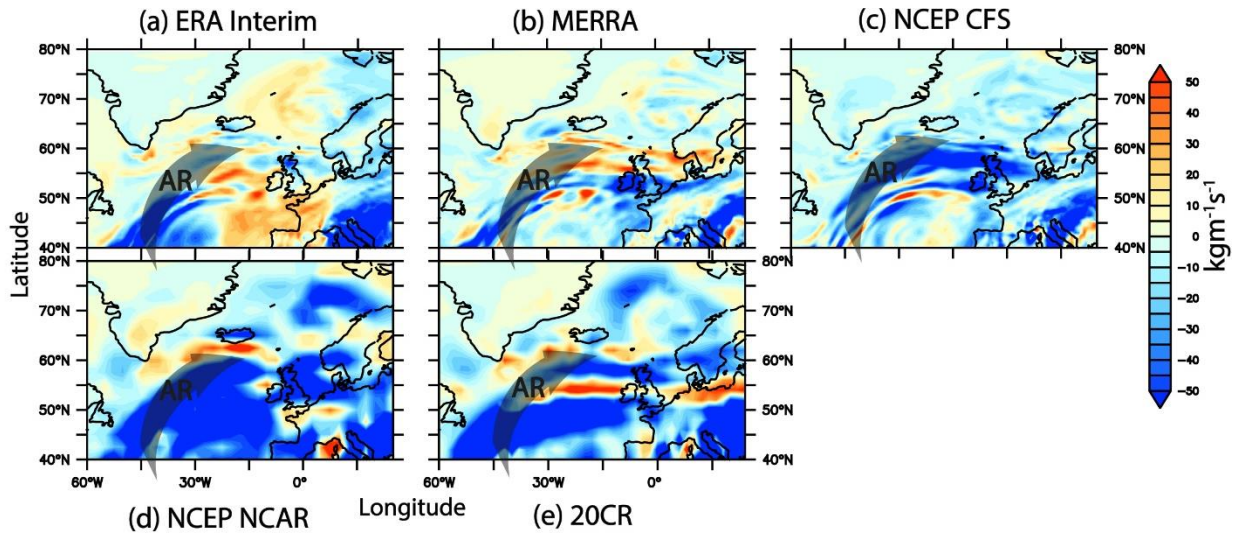
Figure 3: Climatology (coloured areas) and standard deviation (magenta lines) of IWV300

773

in the North Atlantic from all reanalysis data used in the study

774

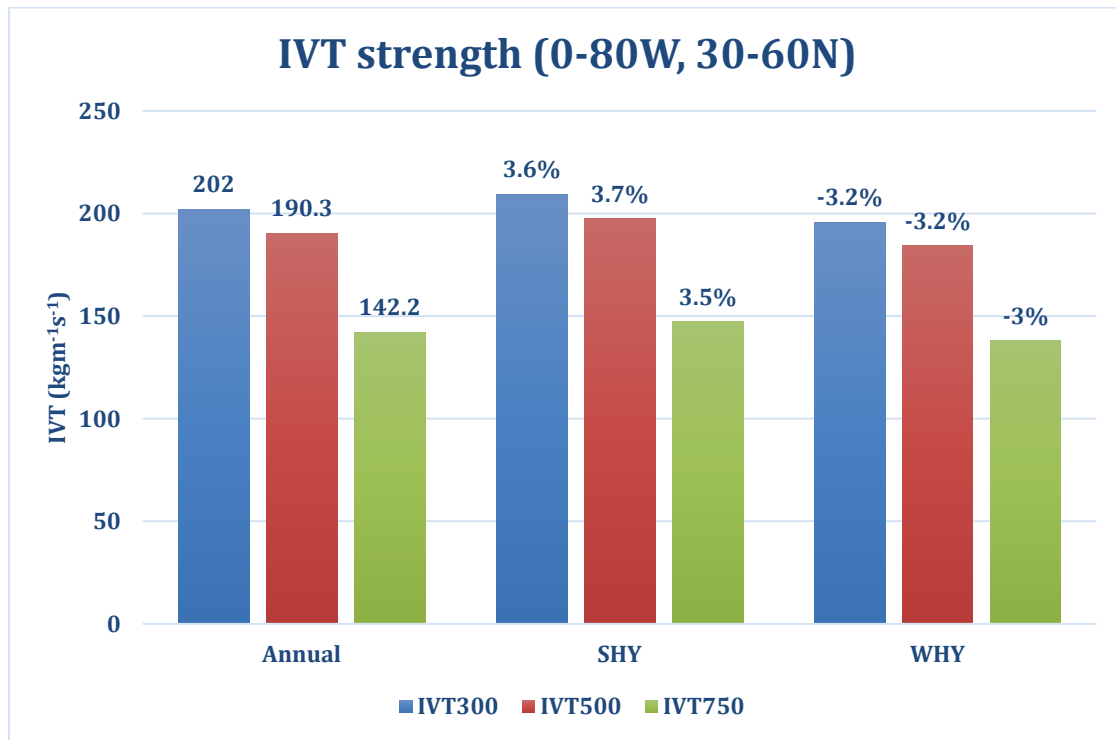
775



776

777 Figure 4: Bias in reanalysis products compared to ERA5 data in mapping AR on 2002 March 06  
 778 using IVT300 algorithm. AR path indicated by a black transparent arrow.

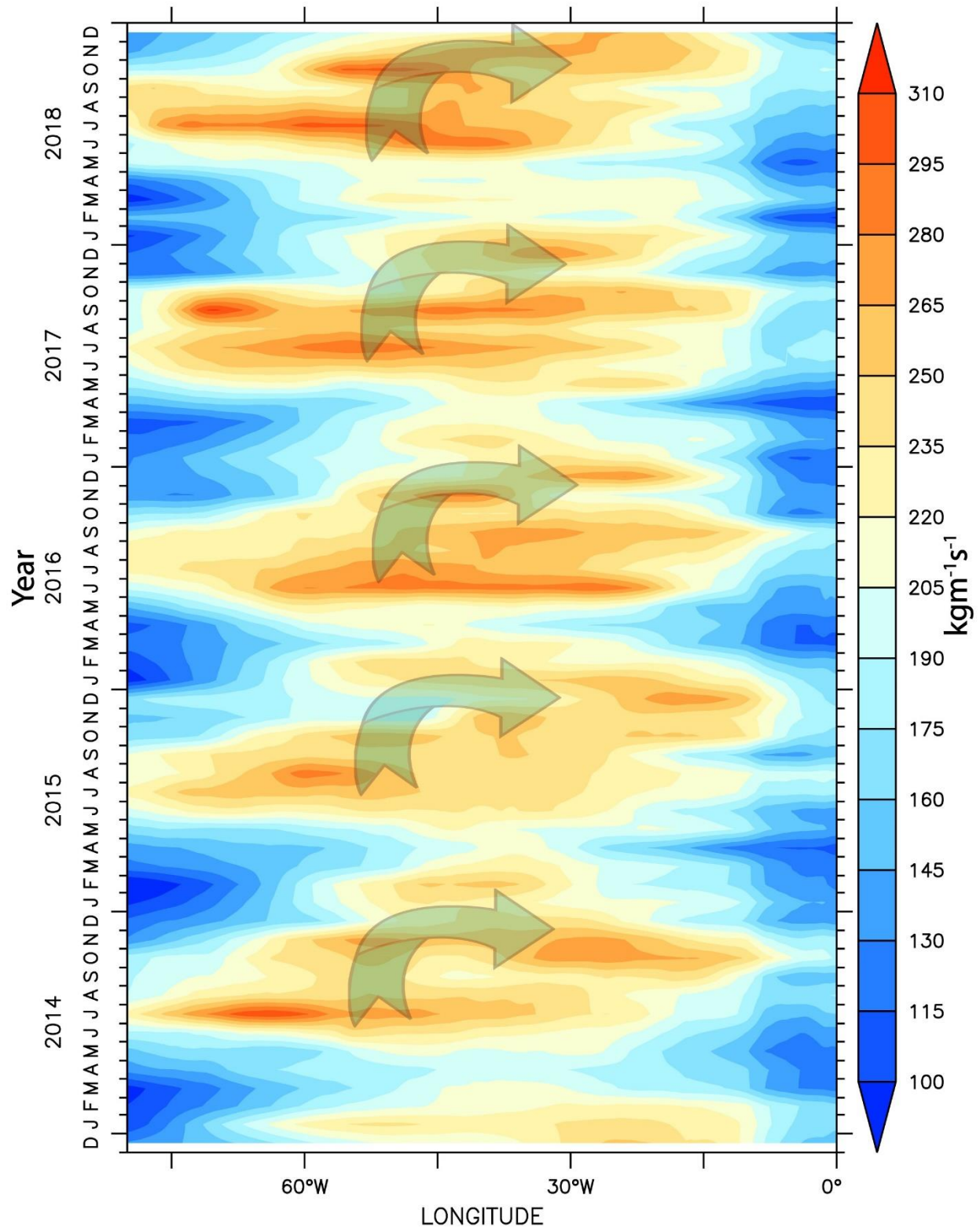
779



780

781 Figure 5: Strength of annual, SHY and WHY mean IVT (kgm<sup>-1</sup>s<sup>-1</sup>) in different layers

782



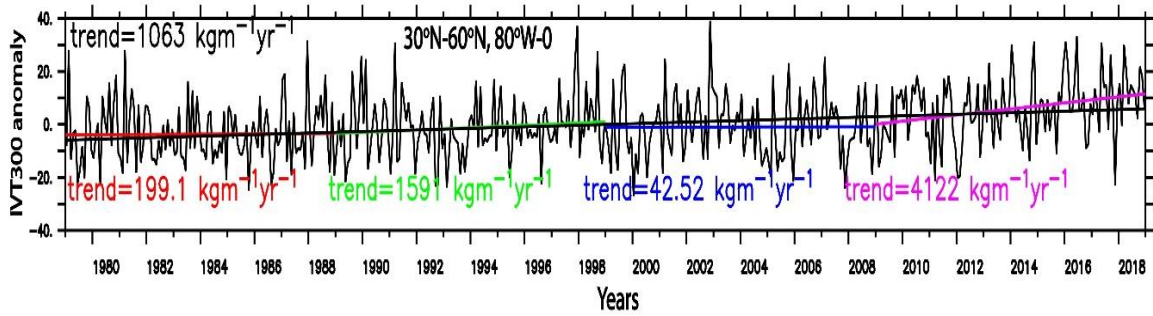
783

784

Figure 6: IVT300 monthly variability along 80°W-0 during 2014-2018

785

786

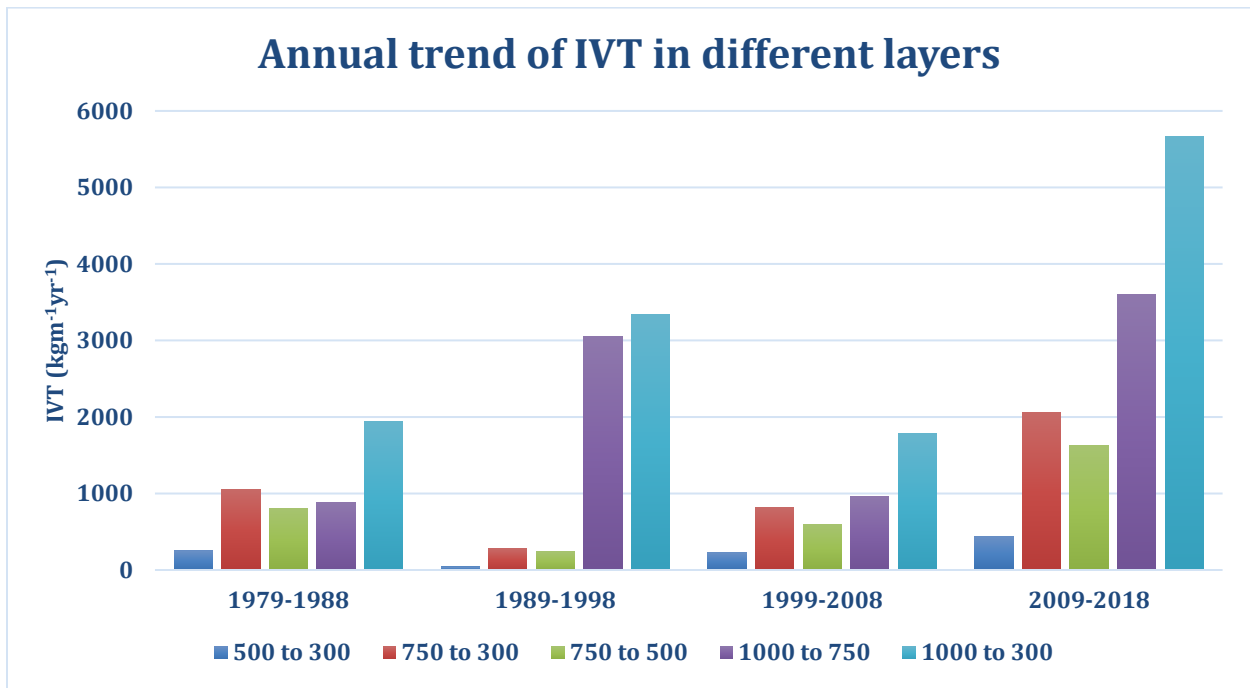


787

788 Figure 7: Decadal trend of IVT300 daily anomaly averaged in the central North Atlantic (30°N-

789

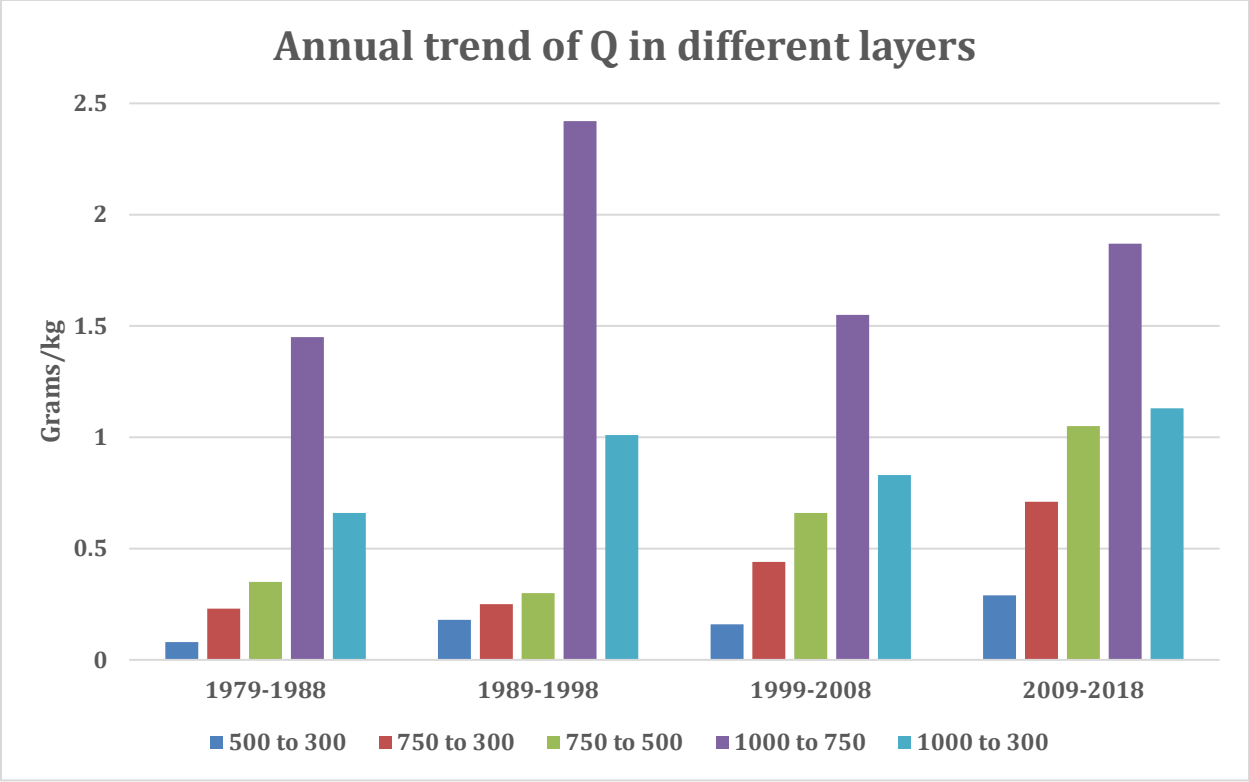
60°N, 80°W-0).



790

791

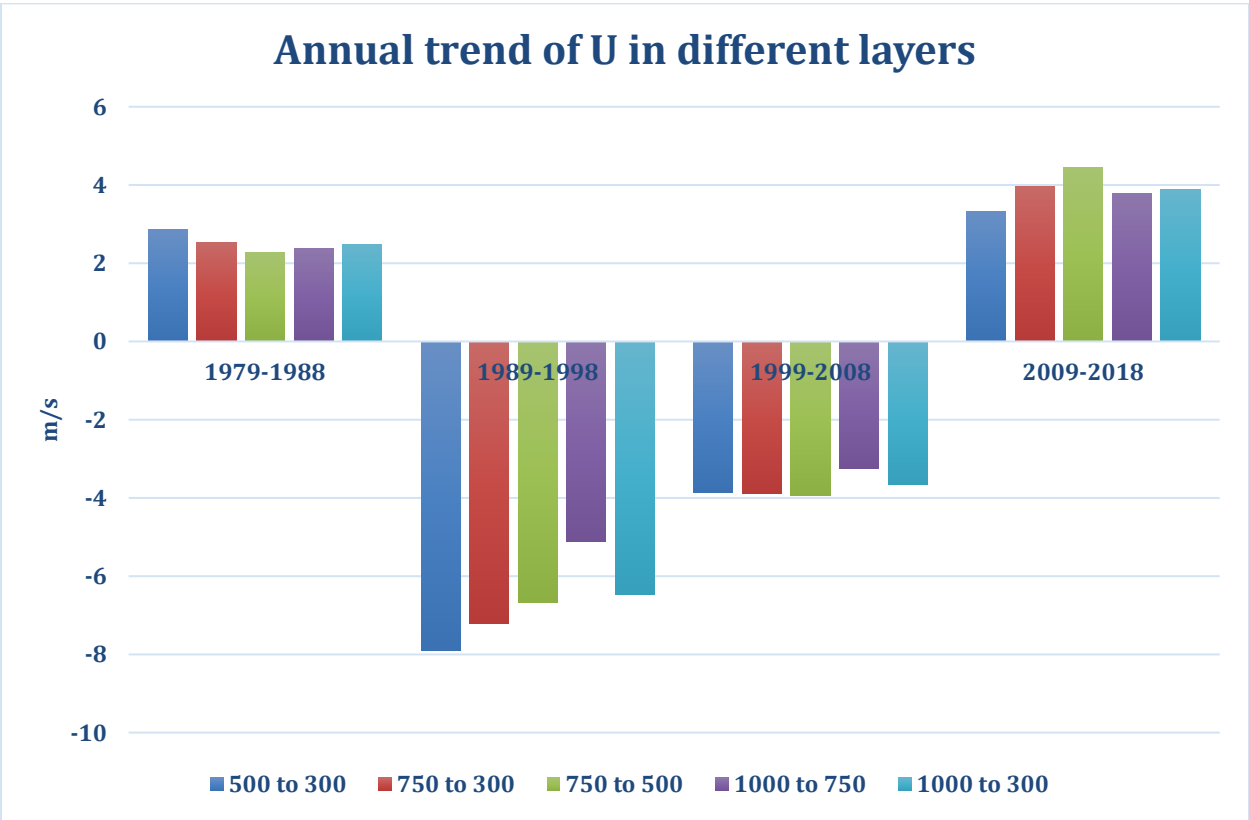
(a)



792

793

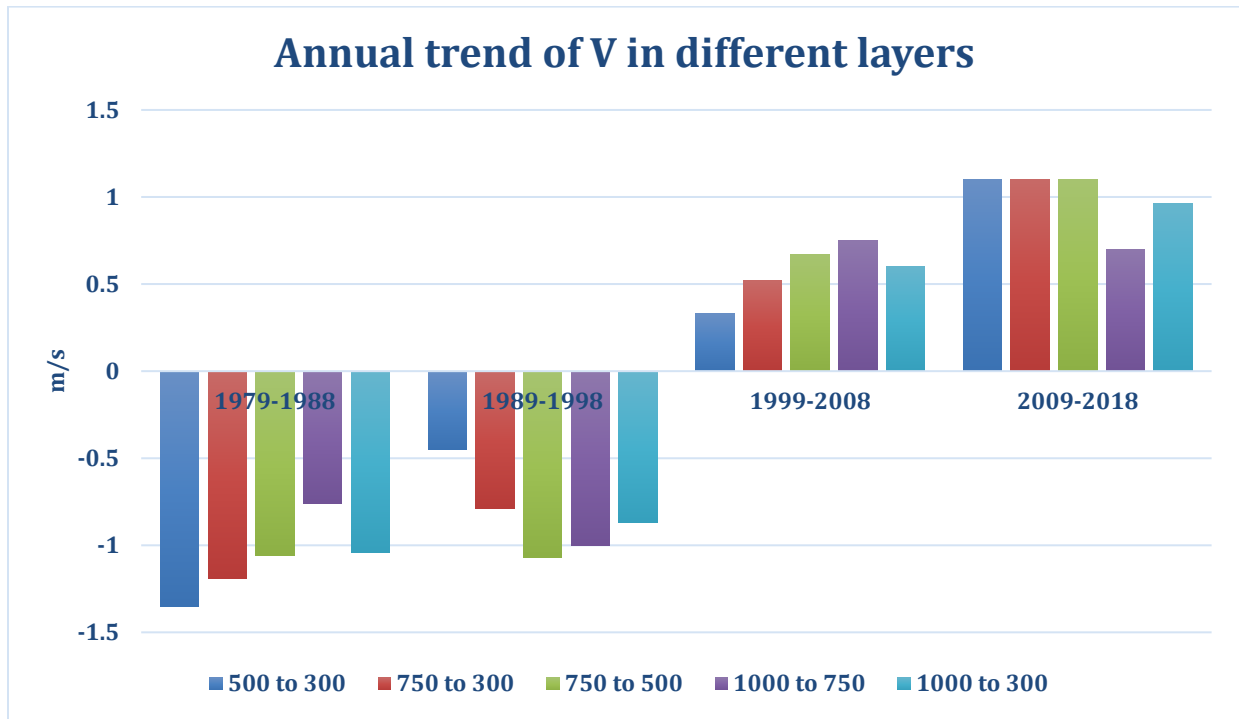
(b)



794

795

(c)



796

797

(d)

798 Figure 8: Decadal trend (significant at 95%) and variability of (a) IVT (b) specific humidity (c)

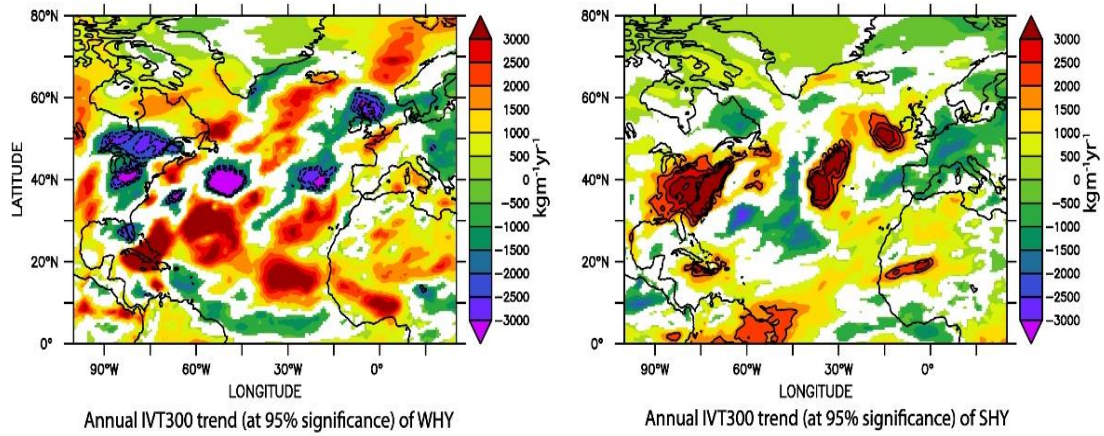
799 zonal wind (d) meridional wind of different layers in the central North Atlantic (30°N-60°N,

800

80°W-0).

801

802

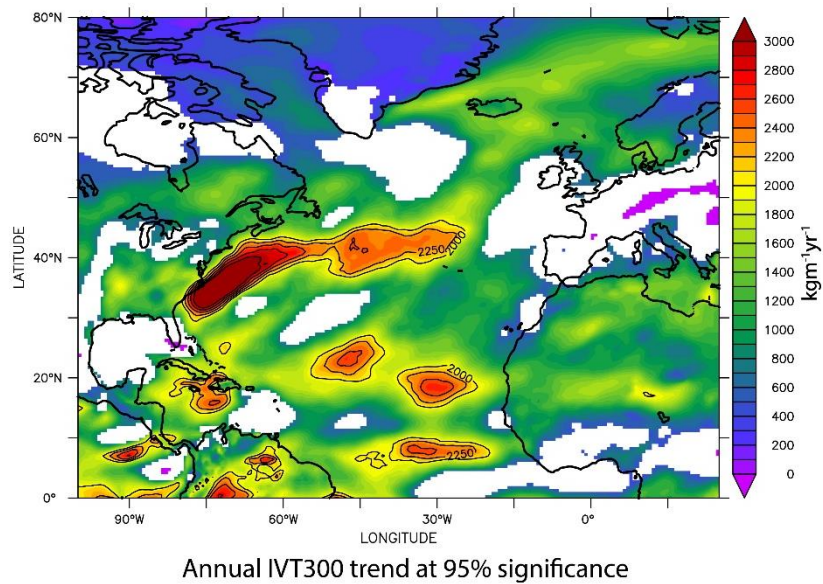


803

804

(a)

(b)



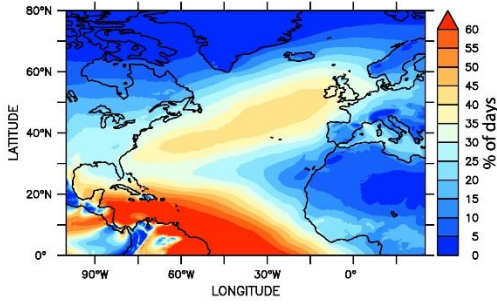
805

806

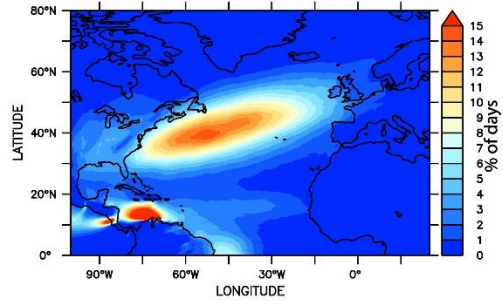
(c)

807 Figure 9: Spatial trend analysis during (a) WHY, (b) SHY and (c) Annual using daily IVT300 (at  
 808 95% significance). White areas indicate no significant trend.

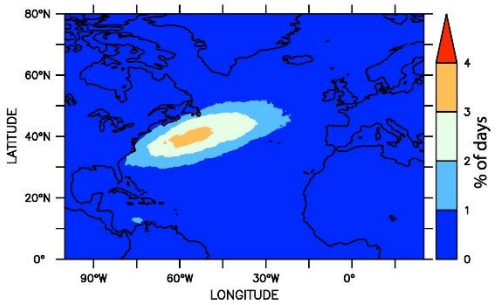
809



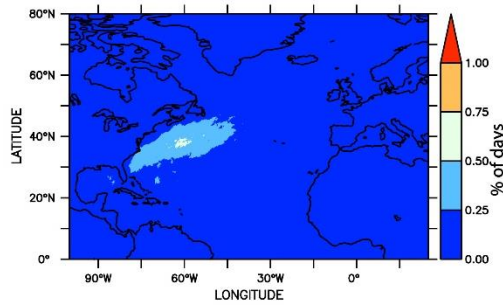
(a) CAT1 IVT300



(b) CAT2 IVT300



(c) CAT3 IVT300



(d) CAT4 IVT300

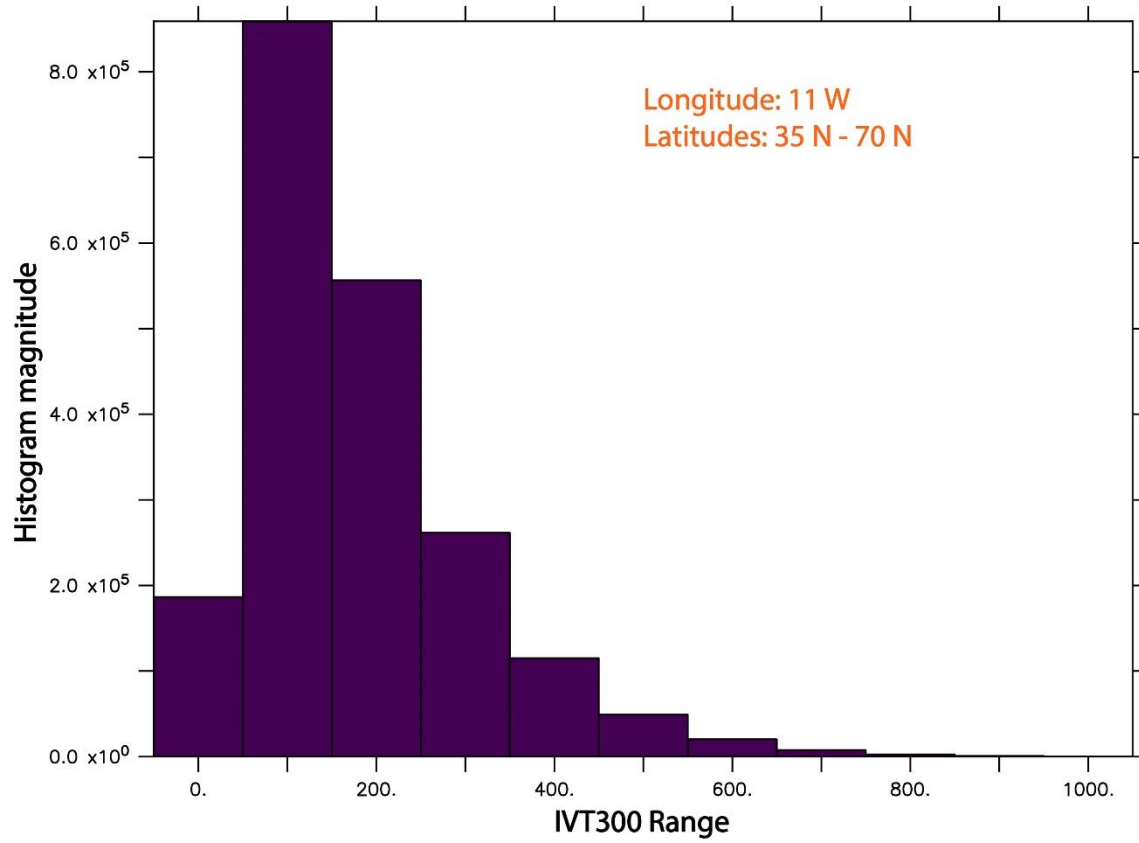
810

811

812

813

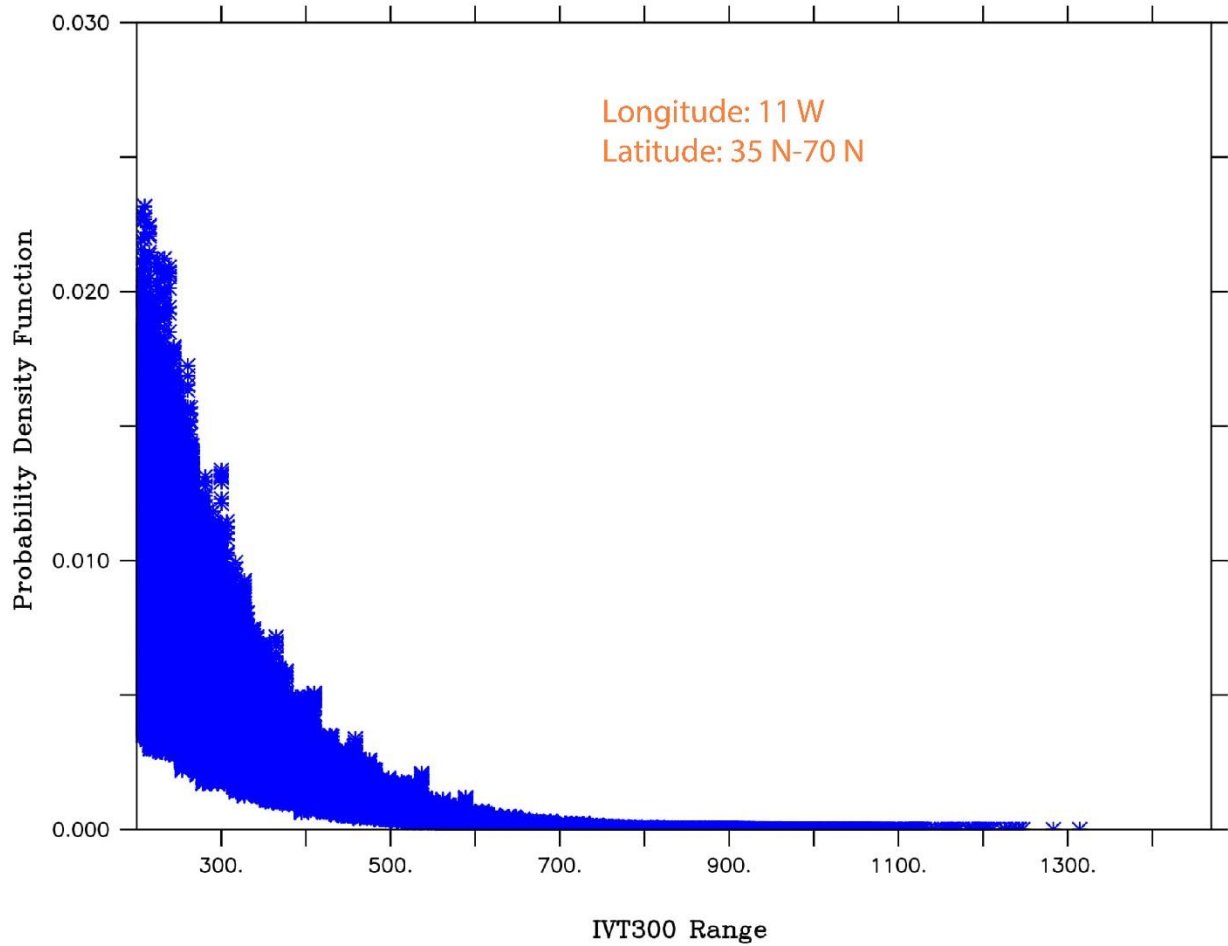
Figure 10: Spatial frequency analysis of different categories of daily IVT300.



814

815

(a)



816

817

(b)

818 Figure 11: (a) Histogram and (b) probability density function of daily IVT300 ( $\text{kgm}^{-1}\text{s}^{-1}$ ) along

819

11°W at latitudes 35-70 N.

820

821

822

823

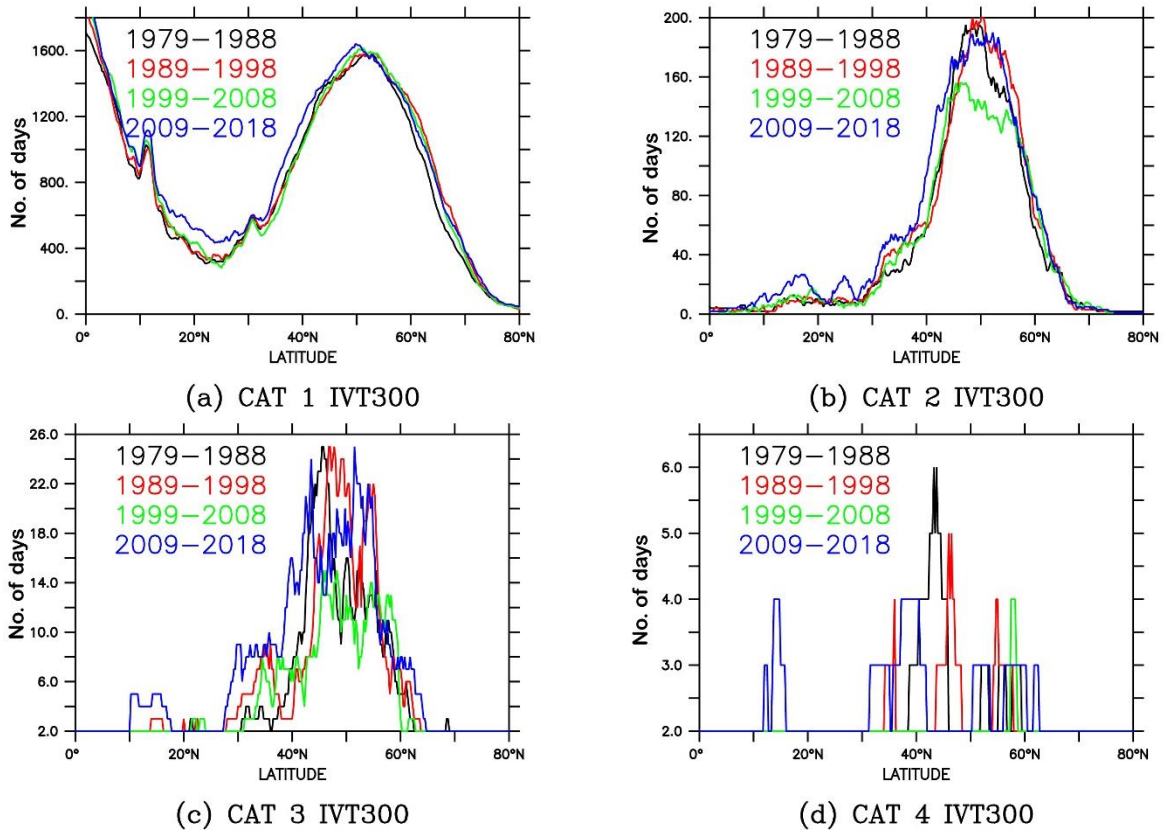
824

825

826

827

828



829

830

831

Figure 12: Frequency of daily IVT300 ( $\text{kgm}^{-1}\text{s}^{-1}$ ) along  $11^\circ\text{W}$ .

832

833

834

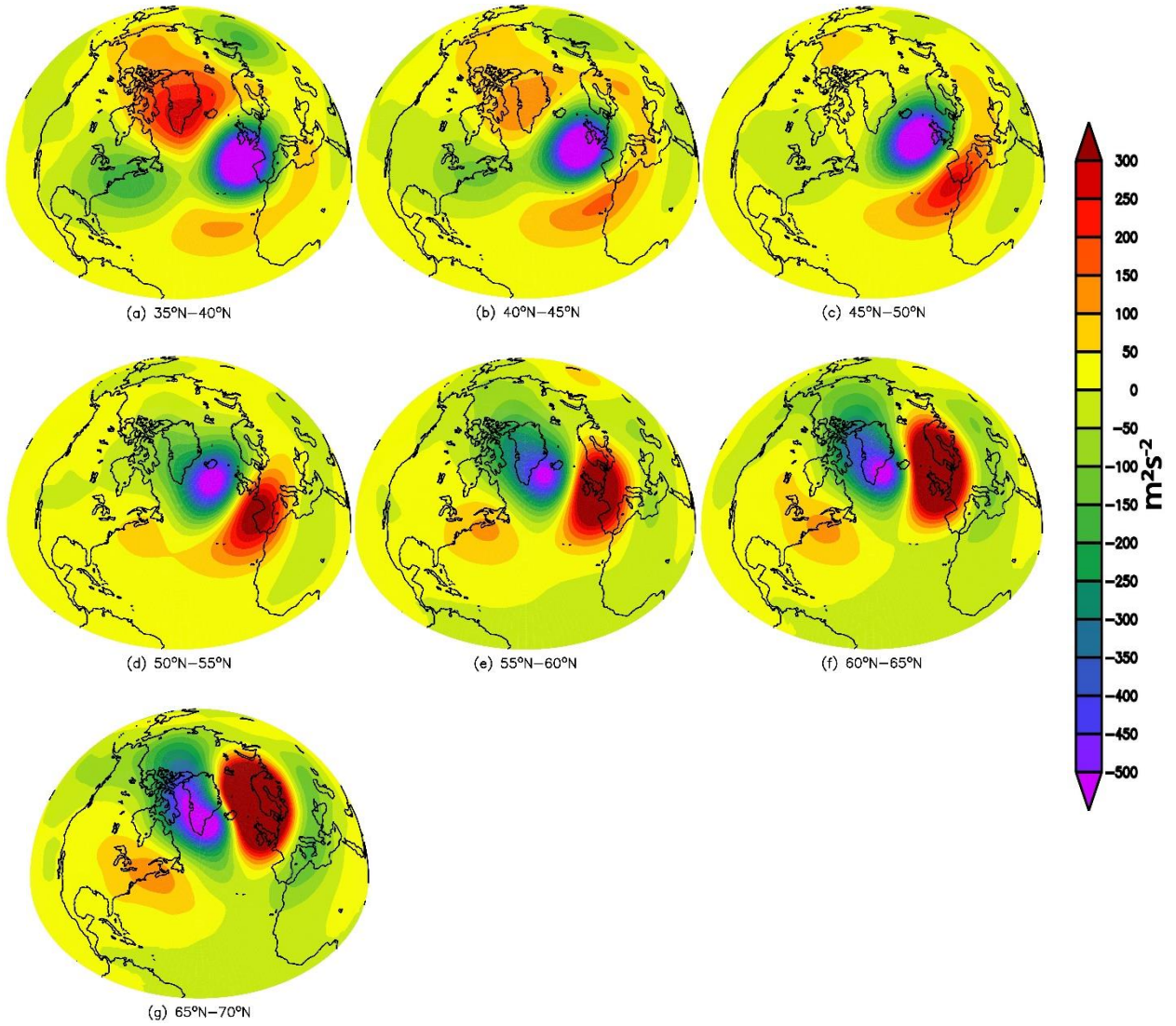
835

836

837

838

839



840

841

842

843

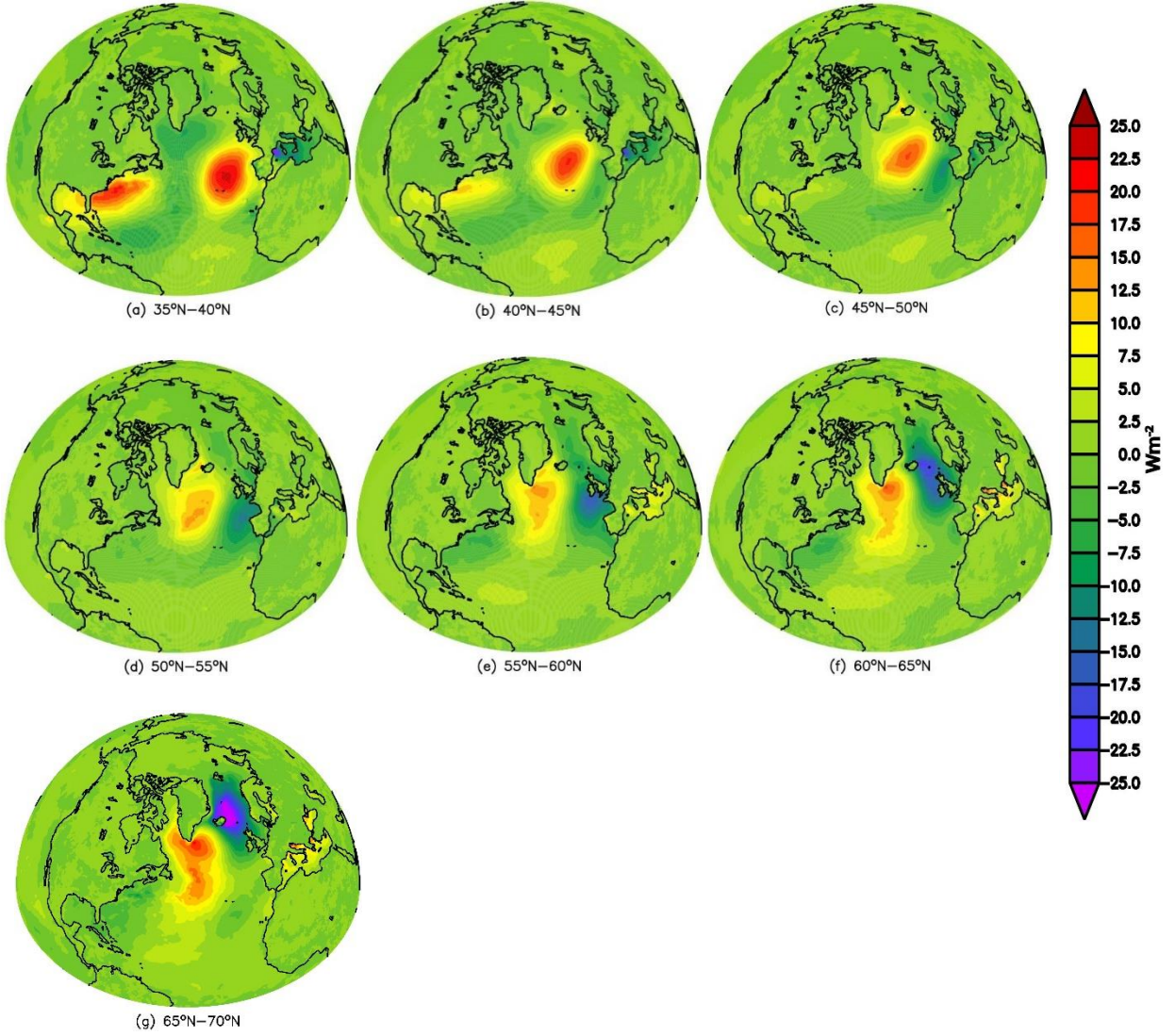
844

845

846

847

Figure 13: Composite of geopotential anomaly along 11°W using different bins



848

849

850

851

852

853

854

Figure 14: Composite of surface latent heat flux anomaly along 11°W using different bins

# Figures

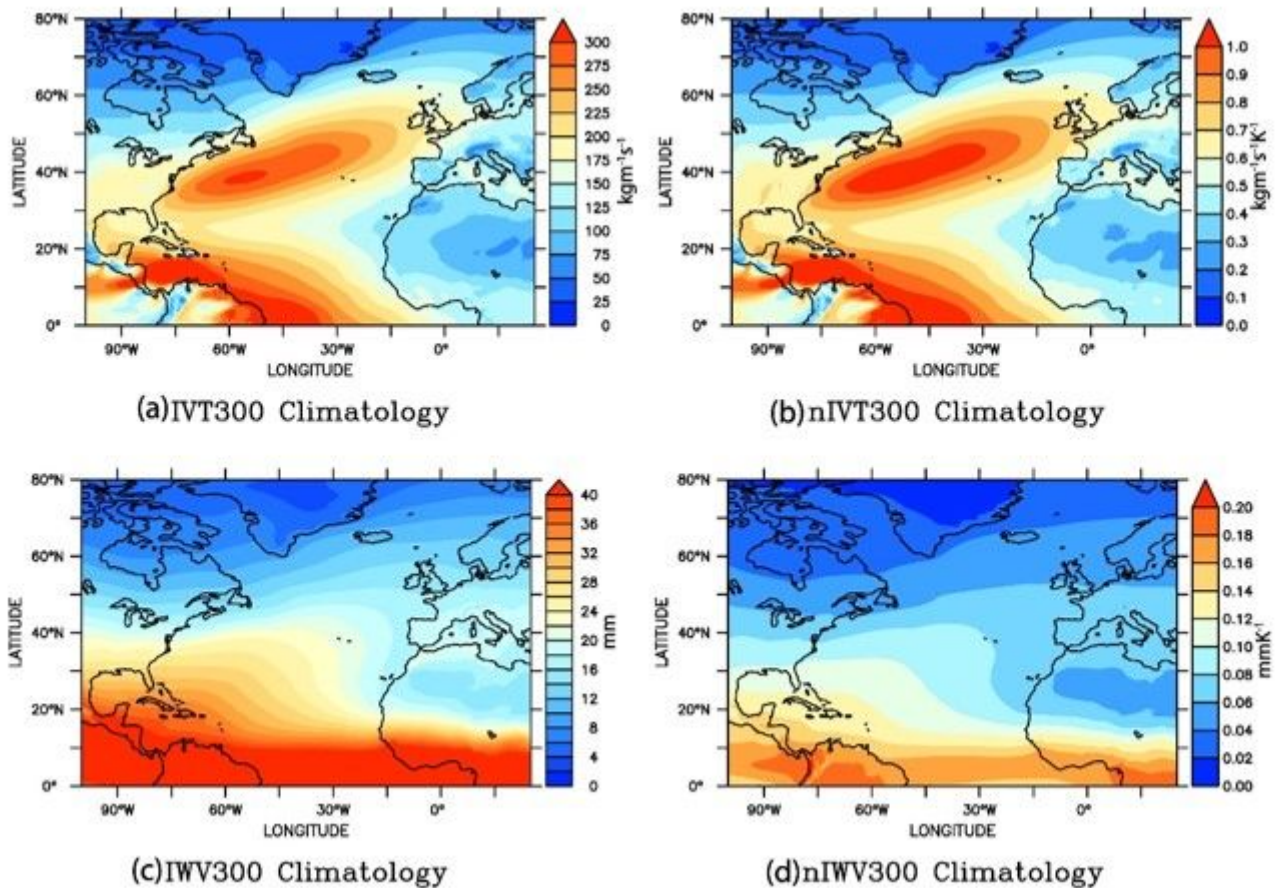
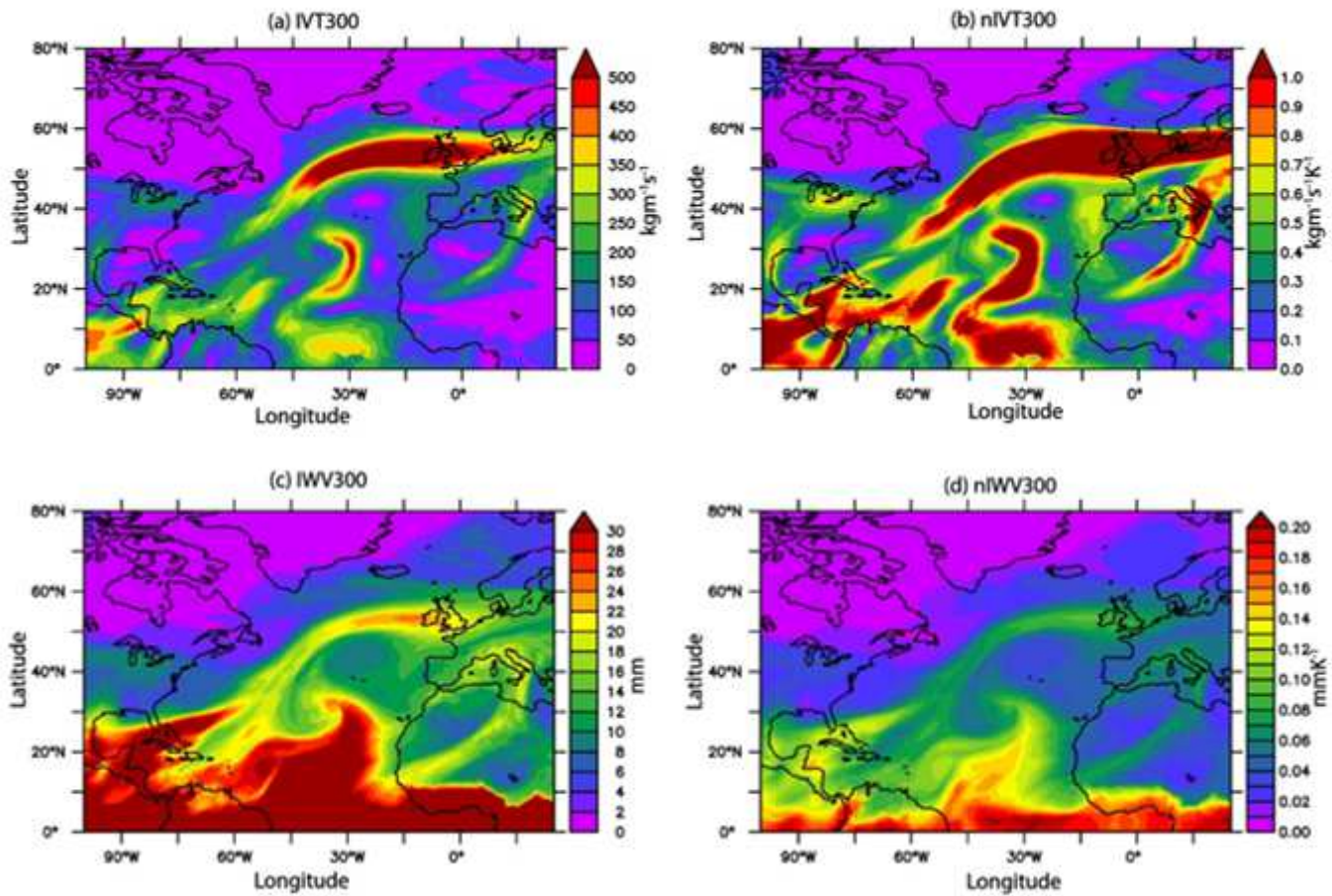


Figure 1

Climatology of ARs computed from daily ERA5 data using four different methods in the north Atlantic. One example of an AR from 6th March 2002 mapped using four different methods in Figure 2 has IVT300 higher than  $500 \text{ kgm}^{-1}\text{s}^{-1}$  (Figure 2a). This event was one of the intense ARs occurred over northern Europe and caused excess rainfall over Britain and southern Scandinavia. While the IVT300 is narrow and short, nIVT300 (Figure 2b) shows the adjacent regions saturated with water vapour. The advected moisture from these surrounding regions could enhance the intensity and lifetime of the AR over a given location. Thus, nIVT300 is a useful method in mapping the true characteristics and saturated water vapour content in AR. Similarly, IWV300 and nIWV300 (Figures 2c, 2d) for this event show origin of AR and the source of the advection, which is, in this case, occurred from the warm tropical region (20°N) enriched with high specific humidity.



**Figure 2**

AR event on 2002 March 06 mapped using four different methods in the north Atlantic using ERA5 data.

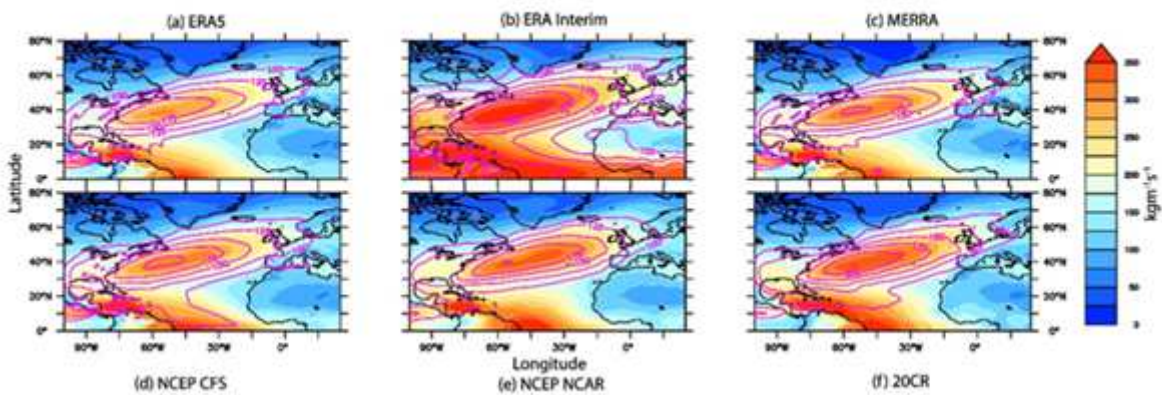


**Figure 3**

Climatology (coloured areas) and standard deviation (magenta lines) of IVT300 in the North Atlantic from all reanalysis data used in the study

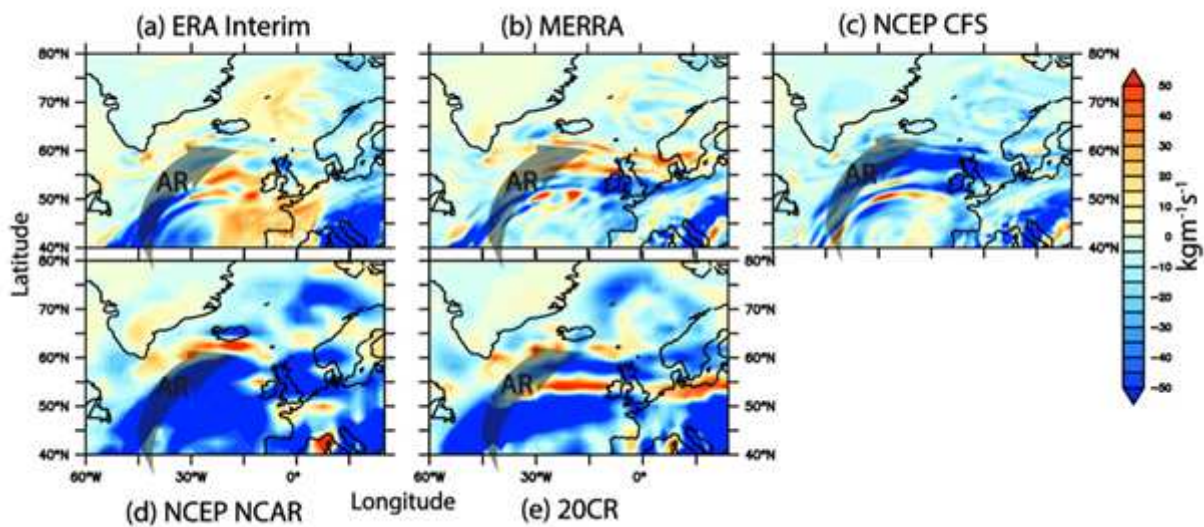


Figure 4

Bias in reanalysis products compared to ERA5 data in mapping AR on 2002 March 06 using IVT300 algorithm. AR path indicated by a black transparent arrow.

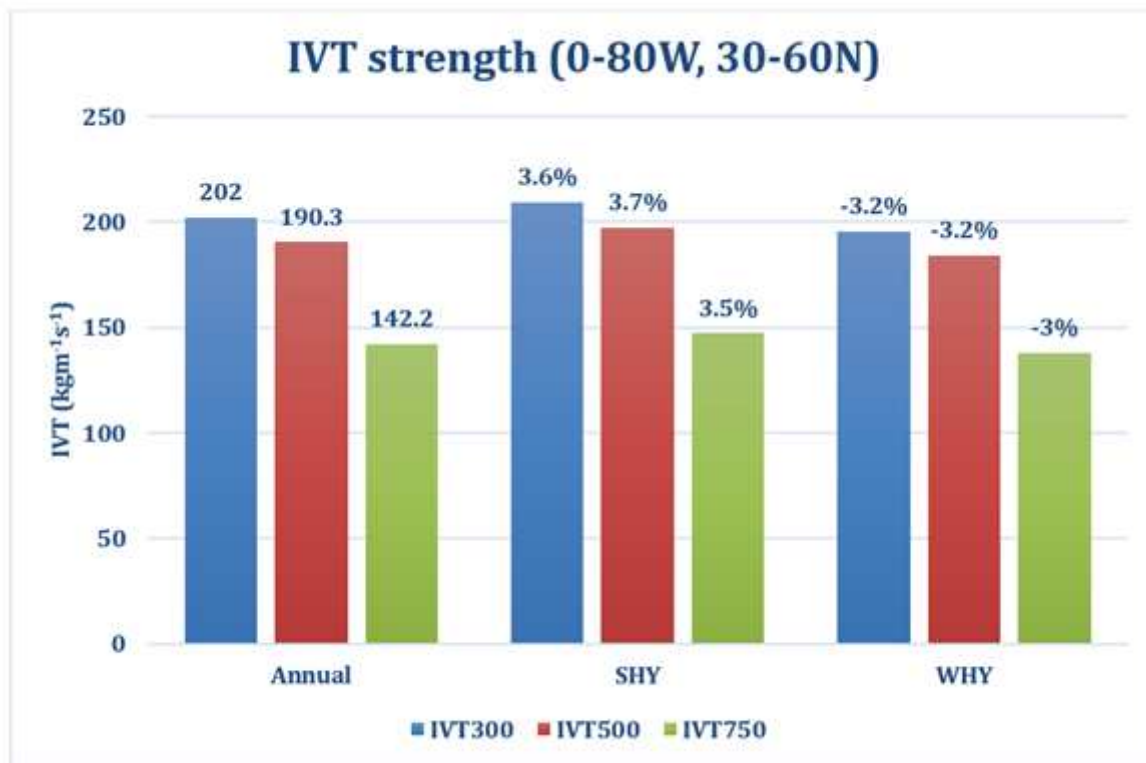
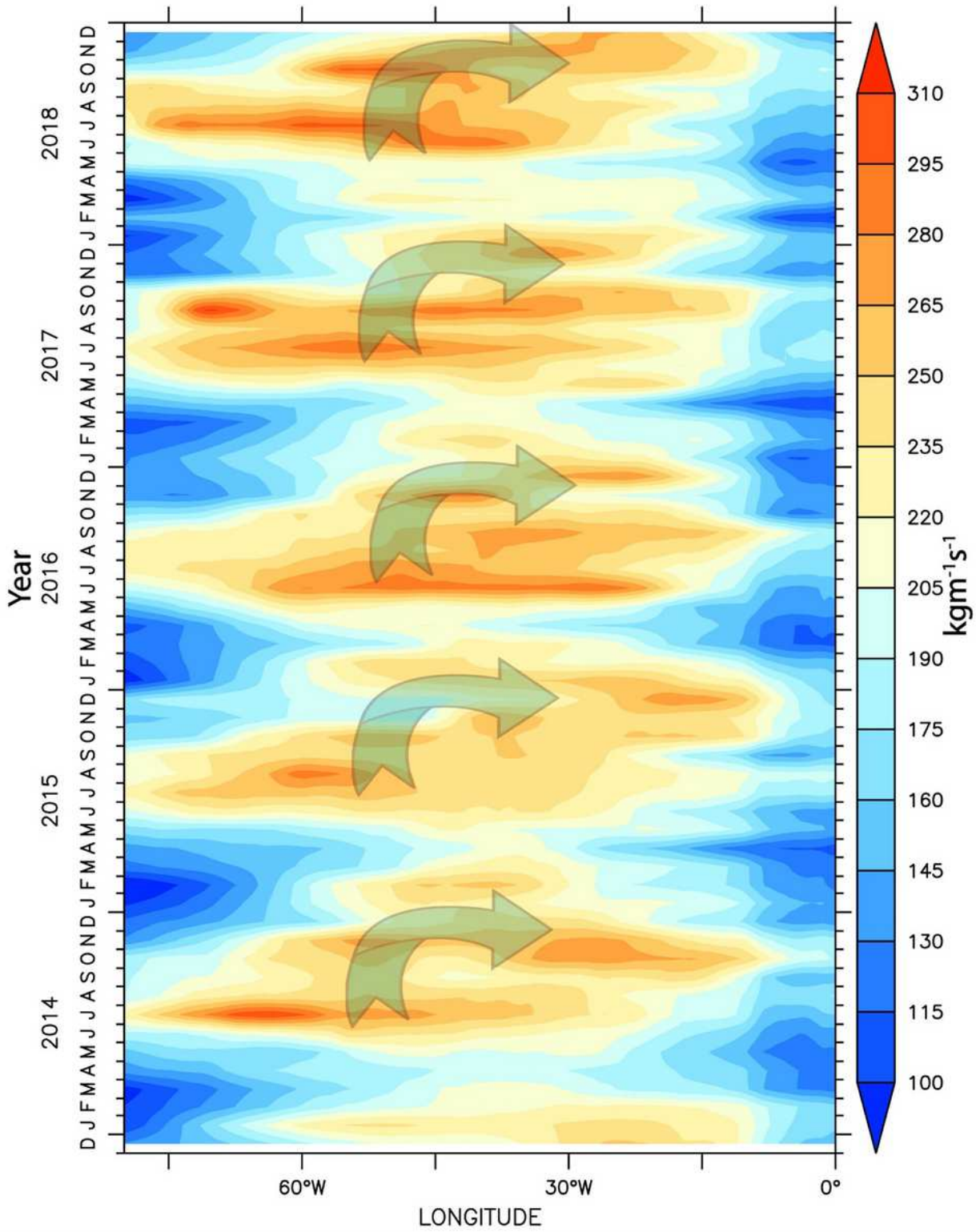


Figure 5

Strength of annual, SHY and WHY mean IVT (kgm<sup>-1</sup>s<sup>-1</sup>) in different layers



**Figure 6**

IVT300 monthly variability along 80°W-0° during 2014-2018

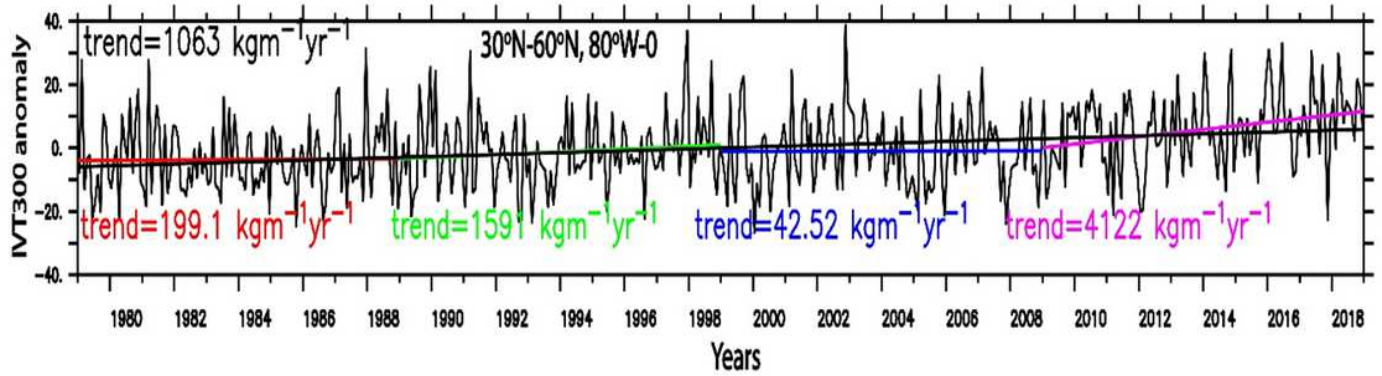


Figure 7

Decadal trend of IVT300 daily anomaly averaged in the central North Atlantic (30oN-60oN, 80oW-0).

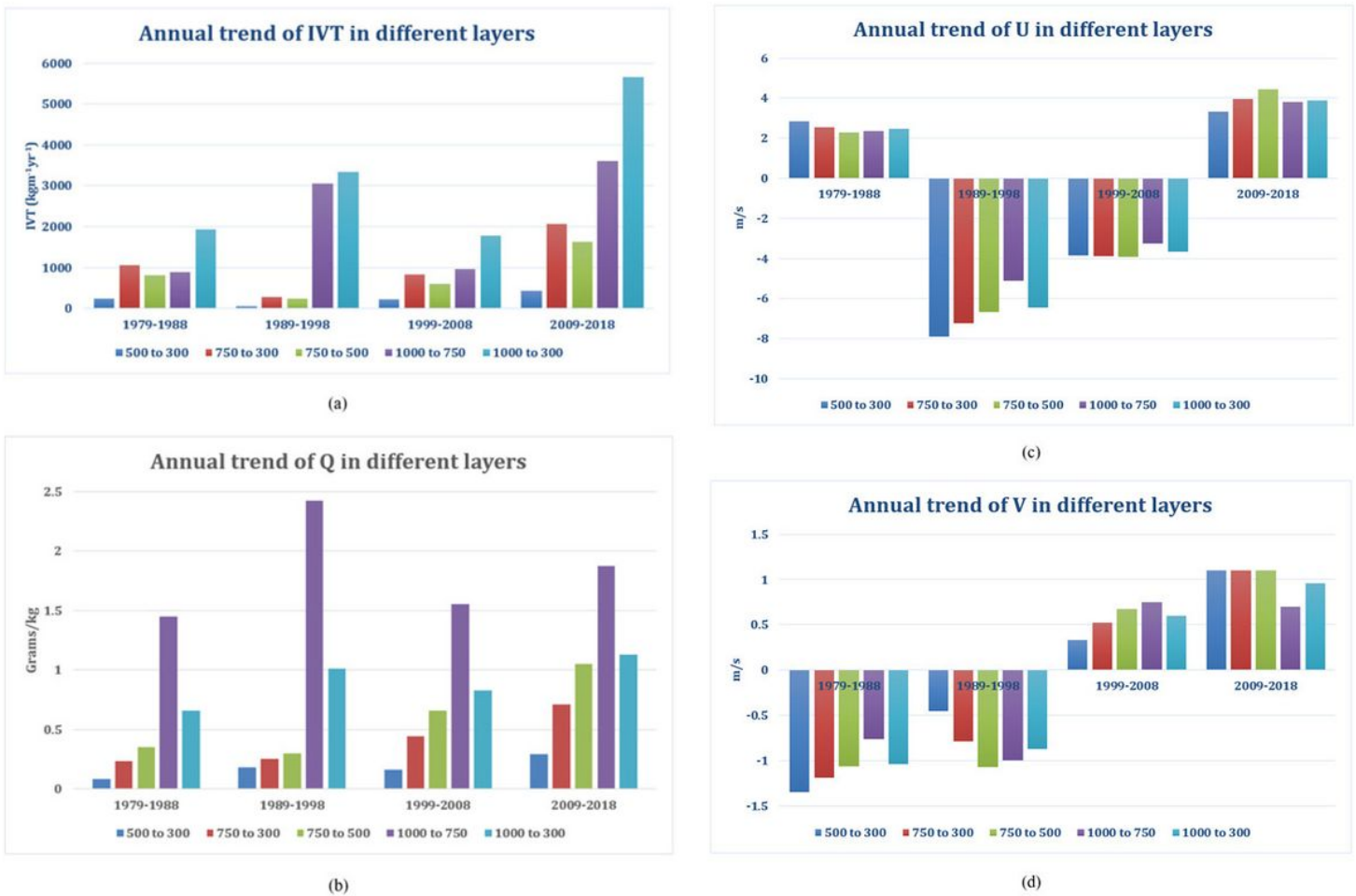
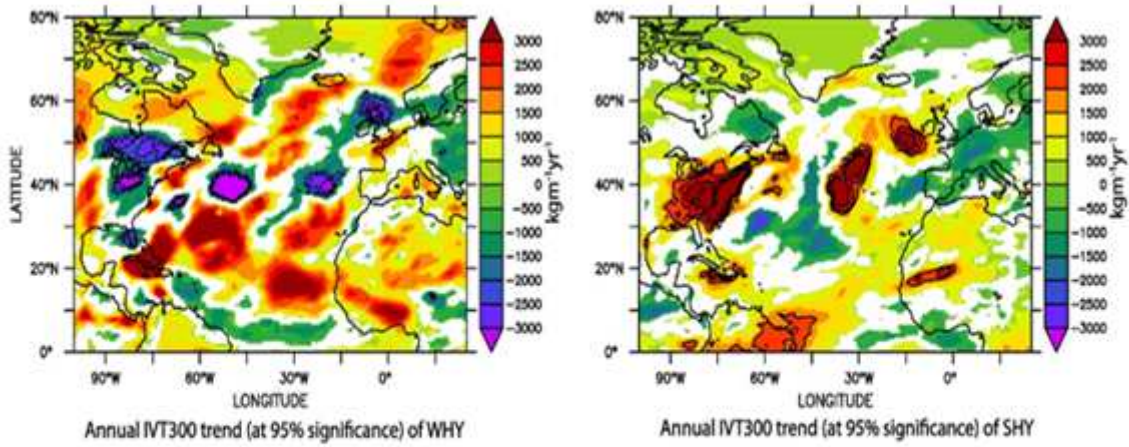


Figure 8

Decadal trend (significant at 95%) and variability of (a) IVT (b) specific humidity (c) zonal wind (d) meridional wind of different layers in the central North Atlantic (30oN-60oN, 80oW-0).



(a)

(b)

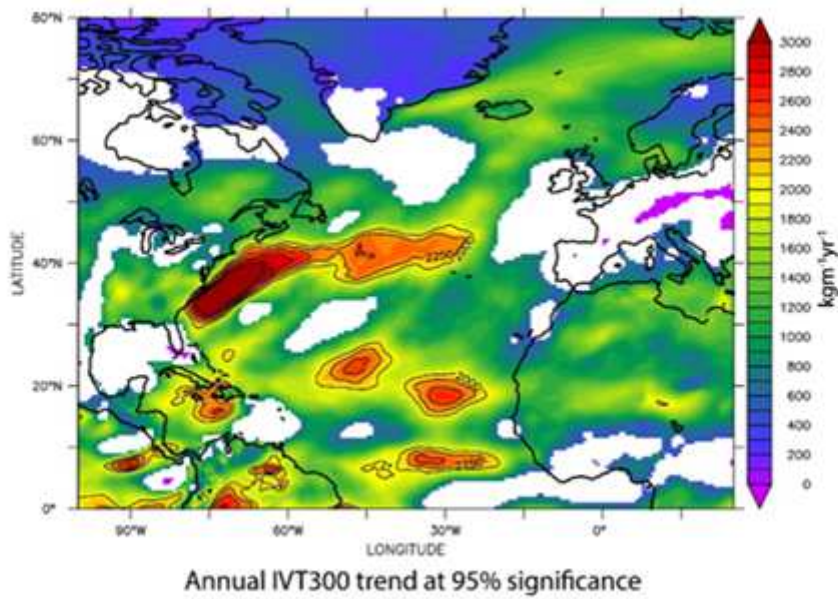


**Figure 9**

Spatial trend analysis during (a) WHY, (b) SHY and (c) Annual using daily IVT300 (at 95% significance). White areas indicate no significant trend.

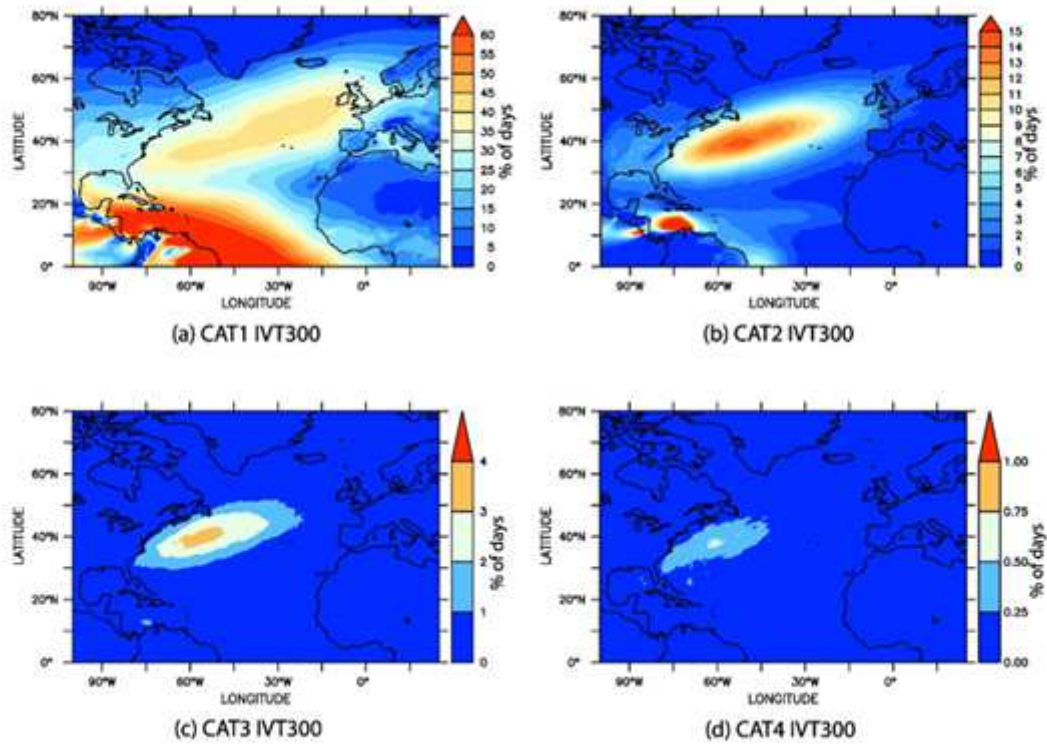
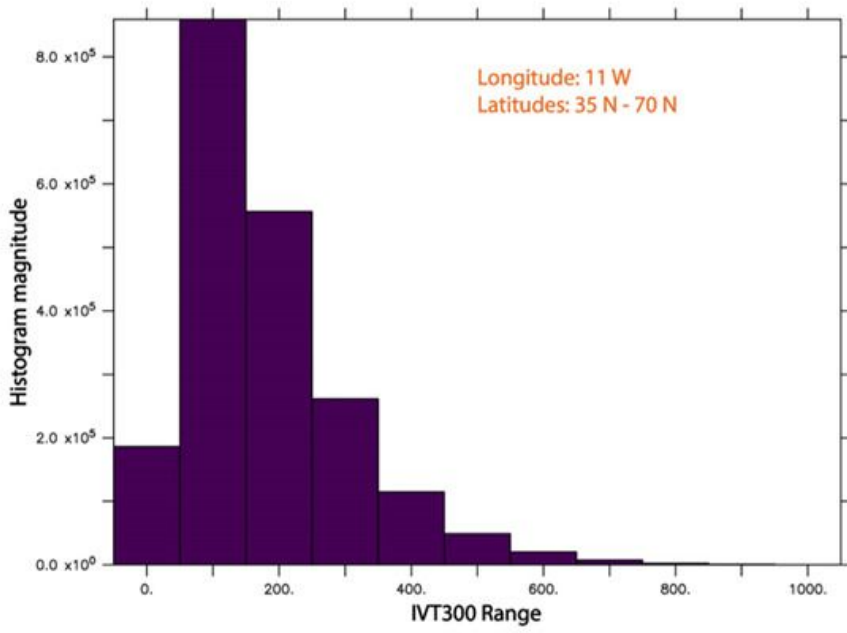
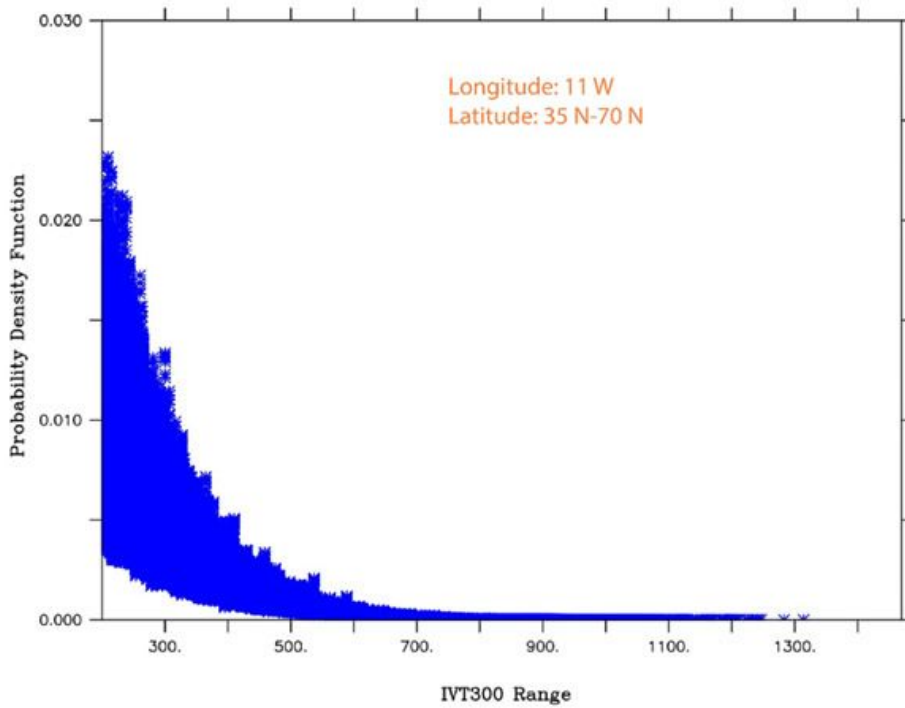


Figure 10

Spatial frequency analysis of different categories of daily IVT300.



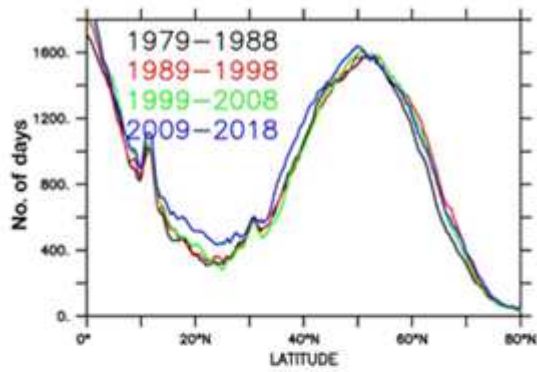
(a)



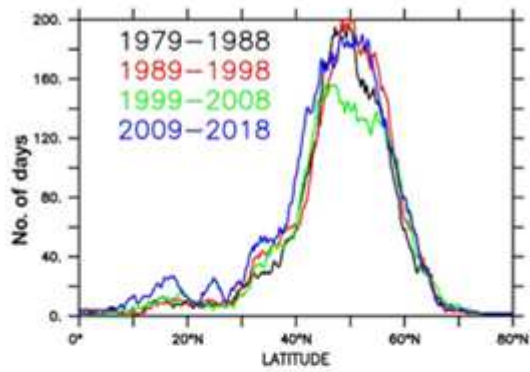
(b)

Figure 11

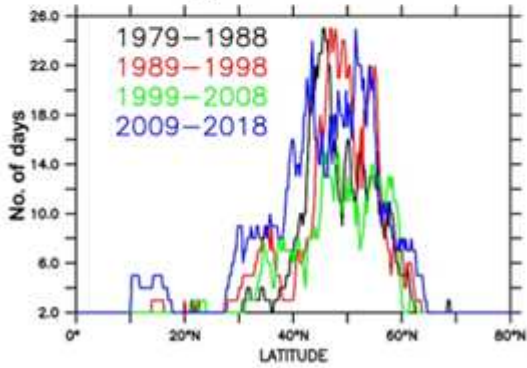
(a) Histogram and (b) probability density function of daily IVT300 ( $\text{kgm}^{-1}\text{s}^{-1}$ ) along 11oW at latitudes 35-70 N.



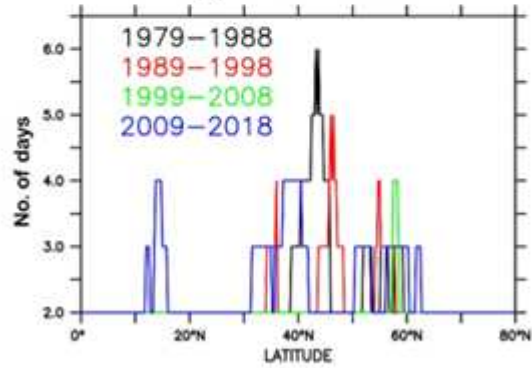
(a) CAT 1 IVT300



(b) CAT 2 IVT300



(c) CAT 3 IVT300



(d) CAT 4 IVT300

Figure 12

Frequency of daily IVT300 ( $\text{kgm}^{-1}\text{s}^{-1}$ ) along 110W.

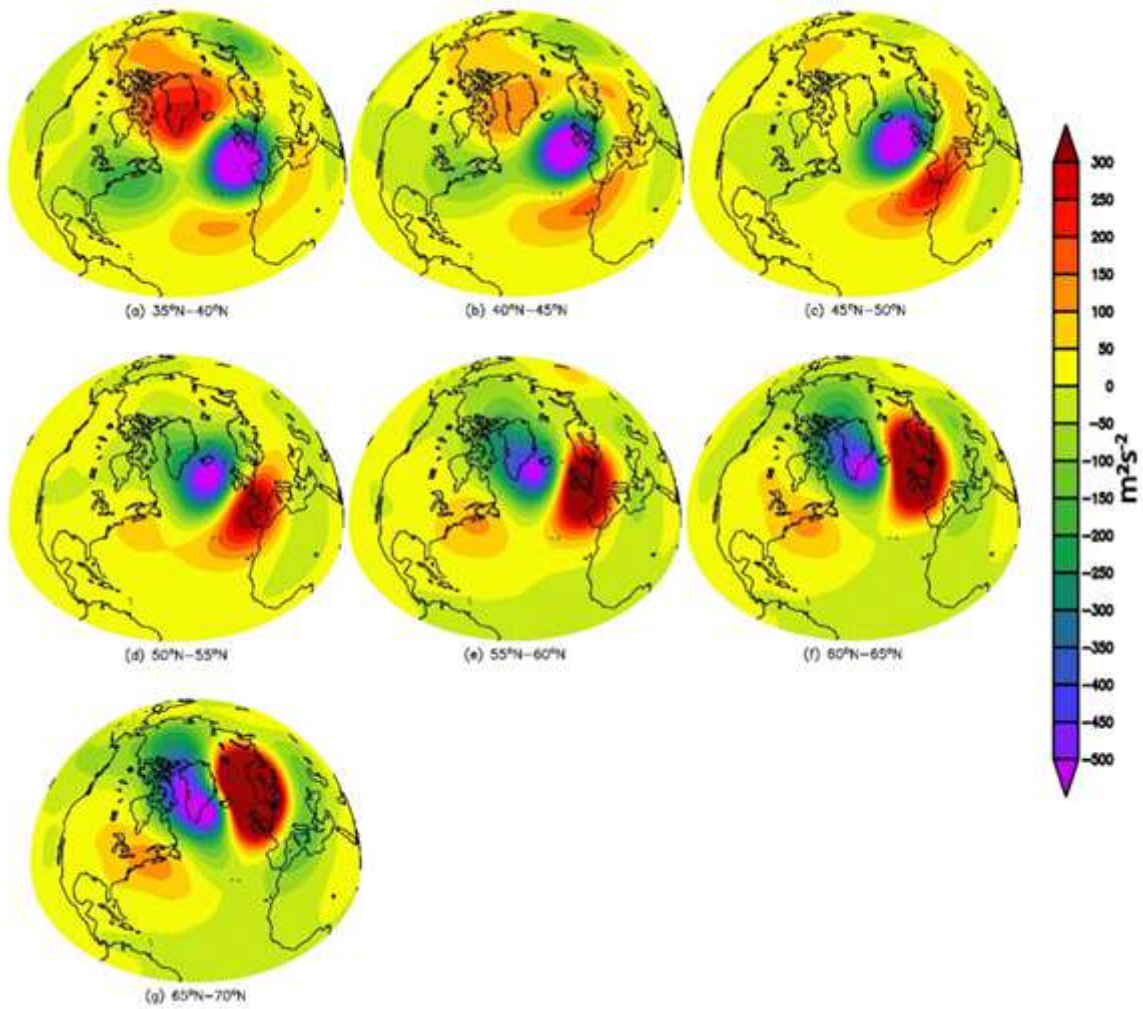


**Figure 13**

Composite of geopotential anomaly along 110W using different bins

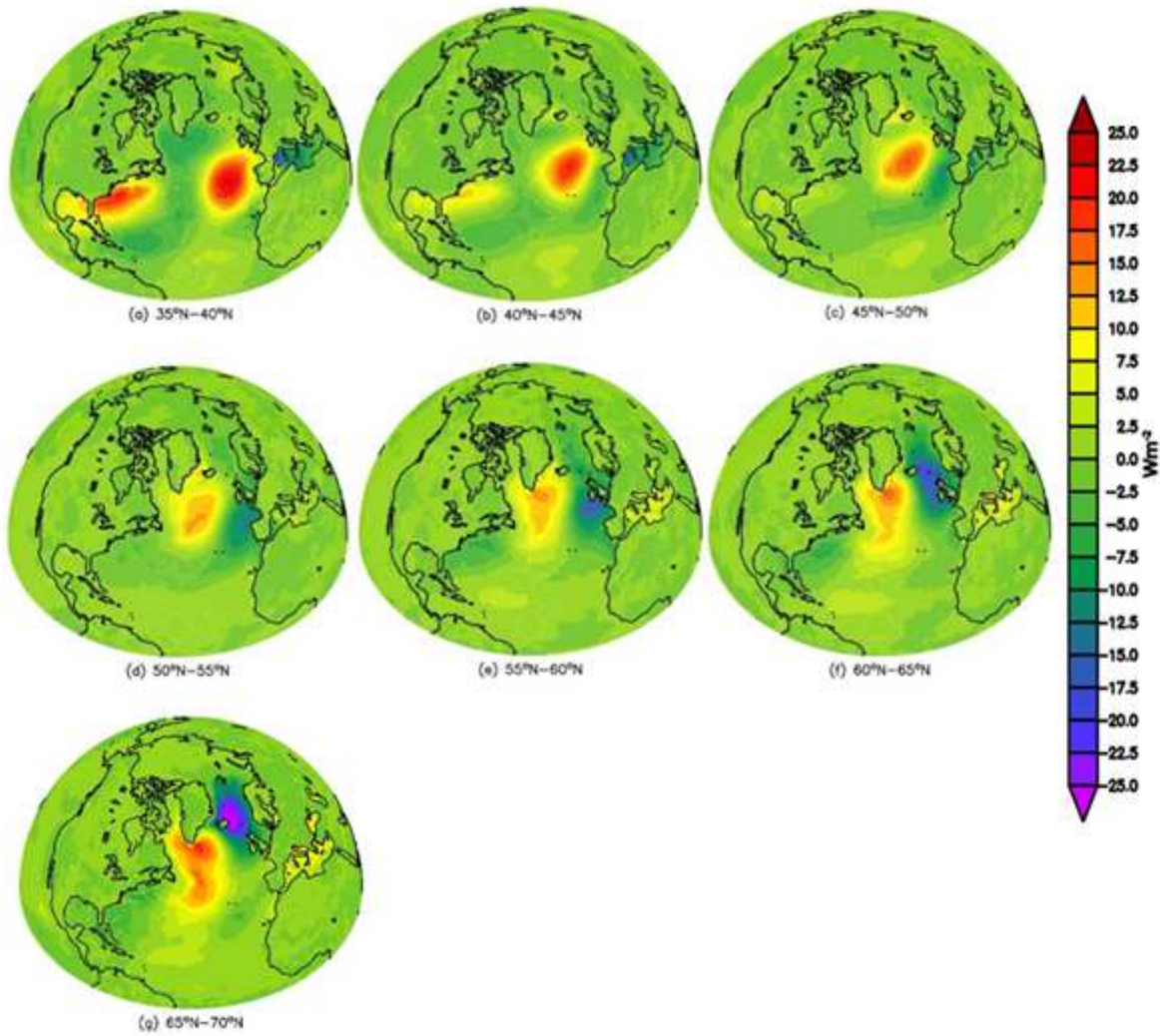


**Figure 14**

Composite of surface latent heat flux anomaly along 11oW using different bins

## Supplementary Files

This is a list of supplementary files associated with this preprint. Click to download.

- [FigureS1.jpg](#)
- [FigureS2.jpg](#)
- [FigureS3.jpg](#)
- [Supplimentarymaterial.docx](#)